A HIGH-RESOLUTION MASS MAP OF GALAXY CLUSTER SUBSTRUCTURE: LensPerfect ANALYSIS OF A1689

DAN COE[1], NARCISO BENÍTEZ[2], TOM BROADHURST[3], AND LEONIDAS A. MOUSTAKAS[1]
[1] Jet Propulsion Laboratory, California Institute of Technology, 4800 Oak Grove Dr, MS 169-327, Pasadena, CA 91109, USA; coe@caltech.edu
[2] Instituto de Astrofísica de Andalucía (CSIC), Camino Bajo de Huétor 50, Granada 18008, Spain
[3] School of Physics and Astronomy, Tel Aviv University, Tel Aviv 69978, Israel

ABSTRACT

We present a strong lensing (SL) mass model of A1689 which resolves substructures an estimated 25 kpc across within the central $\sim$400 kpc diameter. We achieve this resolution by perfectly reproducing the observed (strongly lensed) input positions of 168 multiple images of 55 knots residing within 135 images of 42 galaxies. Our model makes no assumptions about light tracing mass, yet we reproduce the brightest visible structures with some slight deviations. A1689 remains one of the strongest known lenses on the sky, with an Einstein radius of $R_E = 47\rlap{.}''0 \pm 1\rlap{.}''2$ (143^{+3}_{-4} kpc) for a lensed source at $z_s = 2$. We find that a single Navarro–Frenk–White (NFW) or Sérsic profile yields a good fit simultaneously (with only slight tension) to both our SL mass model and published weak lensing (WL) measurements at larger radius (out to the virial radius). According to this NFW fit, A1689 has a mass of $M_{\rm vir} = 2.0^{+0.5}_{-0.3} \times 10^{15}\ M_\odot\ h_{70}^{-1}$ ($M_{200} = 1.8^{+0.4}_{-0.3} \times 10^{15}\ M_\odot\ h_{70}^{-1}$) within the virial radius $r_{\rm vir} = 3.0 \pm 0.2$ Mpc h_{70}^{-1} ($r_{200} = 2.4^{+0.1}_{-0.2}$ Mpc h_{70}^{-1}), and a central concentration $c_{\rm vir} = 11.5^{+1.5}_{-1.4}$ ($c_{200} = 9.2 \pm 1.2$). Our SL model prefers slightly higher concentrations than previous SL models, bringing our SL + WL constraints in line with other recent derivations. Our results support those of previous studies which find A1689 has either an anomalously large concentration or significant extra mass along the line of sight (perhaps in part due to triaxiality). If clusters are generally found to have higher concentrations than realized in simulations, this could indicate that they formed earlier, perhaps as a result of early dark energy.

Key words: dark matter – galaxies: clusters: general – galaxies: clusters: individual (A1689) – gravitational lensing: strong – gravitational lensing: weak – methods: data analysis

Online-only material: color figures, figure sets

1. INTRODUCTION

Galaxy clusters are the largest gravitationally bound objects yet to form in our universe and prove interesting to study both intrinsically and toward other ends. Maps of their dark matter and baryons yield insights into structure formation (Umetsu et al. 2009; Kawaharada et al. 2010) and can even constrain the nature of dark matter particles (specifically, their self-interacting cross section; Randall et al. 2008; Feng et al. 2009). Cosmological constraints can be obtained from number counts of clusters with measured masses (Mantz et al. 2009; Vikhlinin et al. 2009; Rozo et al. 2010) or from the observed gravitational lensing of more distant objects with measured redshifts (Gilmore & Natarajan 2009). As the strongest gravitational lenses on our sky, clusters can also be used as cosmic telescopes allowing us to peer further back in time to reveal galaxies in the distant ($z \gtrsim 7$) universe (Bradley et al. 2008; Richard et al. 2008) or study galaxies at "modest" redshifts ($z \sim 3$–5) in greater detail (Bunker et al. 2000; Frye et al. 2007, 2008).

By mapping the dark matter distributions within galaxy clusters (as projected on our sky), gravitational lensing analyses have yielded many exciting (and at times controversial) findings, from the Bullet Cluster (Markevitch et al. 2004; Clowe et al. 2006; Randall et al. 2008) to the "dark matter ring" in CL0024 (Jee et al. 2007) and the "cosmic train wreck" in A520 (Mahdavi et al. 2007). These results are exciting in part because they reveal the distribution of dark matter without assuming that light traces mass (hereafter "LTM"[4]).

Similarly exciting dark matter maps can now be obtained in finer detail in galaxy cluster cores thanks to strong gravitational lensing (hereafter, SL) analysis of high-quality data. The galaxy cluster A1689 is one of the strongest gravitational lenses on our sky,[5] with an Einstein radius of $R_E \sim 47''$ for a background object at $z_s = 2$. Deep (20-orbit) multiband Advanced Camera for Surveys (ACS) GTO observations of this cluster reveal over 100 strongly lensed multiple images of 30 background galaxies (Broadhurst et al. 2005b), a huge leap forward in the number of SL constraints available for any single massive body. Based on these multiple images (and others identified since), we derive a mass model which resolves substructure an estimated 25 kpc ($8''$) across within the central $\sim$400 kpc ($2'$) diameter (see Section 5.1). If verified, this would be the highest resolution mass model to date of any galaxy cluster without assuming LTM. For comparison, weak lensing (hereafter, WL) mass maps typically resolve structure on $\sim$1′ scales from ground-based imaging or $\sim$45″ from space (Heymans et al. 2008). Of course WL complements SL nicely, as WL probes cluster mass distributions to much larger radii (the virial radius $r_{\rm vir} \gtrsim 2$ Mpc) where the lensing strength is weaker.

Traditional SL analysis methods were not able to fully process the large numbers of multiple images revealed in the ACS images of A1689. LTM models produced by Broadhurst et al. (2005b, hereafter B05), Zekser et al. (2006, hereafter Z06), Halkola et al. (2006, hereafter H06), and Limousin et al. (2007b, hereafter L07) all failed to reproduce the 100+ observed multiple image positions by $\gtrsim 2\rlap{.}''5$ (see Table 1). This is roughly 50 times the observational uncertainties of 1 pixel or so ($\sim$0$\rlap{.}''$05). By

Q1

---

[4] We will avoid describing models as "parametric" or "non-parametric," since strictly speaking all mass models do have parameters. Here, we introduce the more important distinction between "LTM" and "non-LTM" models.

[5] See Zitrin et al. (2009a) for the current strongest gravitational lens.

Table 1
Published Strong Lensing Mass Reconstructions of A1689 Based on the ACS Images

Alias	Paper	Assume LTM	Galaxies	Multiple Images	Average Residuals	
					Source Plane	Image Plane[a]
B05	Broadhurst et al. (2005b)	✓	30	106	⋯	$3\overset{''}{.}2$
	Diego et al. (2005b)	×	30	106	⋯	$3''$
Z06	Zekser et al. (2006)	✓	22–30	74–106	$0\overset{''}{.}7$–$1\overset{''}{.}2$	⋯
	Saha et al. (2006)	×	7, 9	28, 30	0	0
H06	Halkola et al. (2006)	✓	31 + arc	107	⋯	$2\overset{''}{.}7$
H07	Halkola et al. (2007)	✓	31 + arc	107	⋯	$2\overset{''}{.}5$
L07	Limousin et al. (2007b)	✓	34	113	$0\overset{''}{.}45$	$2\overset{''}{.}87$
	Jullo & Kneib (2009)	✓ ×[b]	12	28	⋯	$0\overset{''}{.}28$
LP	This paper	×	42	135	0	0

Notes.
[a] Observational uncertainties are $\sim 0\overset{''}{.}05$ in the image plane.
[b] Jullo & Kneib (2009) include both LTM and non-LTM substructure components.

failing to match the tight observational constraints, these models discard a great deal of information available in the quality ACS images.

Despite their greater flexibility, non-LTM models were unable to reduce these residuals given all 100+ multiple images. Diego et al. (2005b), using SLAP,[6] allowed residuals similar to those in LTM models. Saha et al. (2006), using PixeLens, produced non-LTM models which perfectly reproduce some of the data, but computational limitations restrict PixeLens to fitting only 30 multiple images at a time. Similarly, Jullo & Kneib (2009), using a hybrid scheme combining LTM and non-LTM substructure, leave relatively small ($0\overset{''}{.}28$) average residuals, but only for a subset of 28 multiple images.

In this paper, we present non-LTM mass models which perfectly[7] reproduce the observed (lensed) input positions of 168 multiple images of 55 knots residing within 135 images of 42 galaxies. The resolution of a reconstructed mass model is given roughly by the spatial density of the multiple image constraints (Coe et al. 2008; Coe 2009). Thus, our model which incorporates 135 multiple images has $\sim 4\times$ greater spatial resolution ($\sim 2\times$ greater along each axis) than the aforementioned models which incorporate only ~ 30 multiple images.

Our SL analysis method (LensPerfect; Coe et al. 2008) was made possible just recently thanks to the development of mathematical tools enabling one to obtain curl-free interpolations of a vector field which perfectly reproduce the input data at the input positions (Fuselier 2006, 2007). We make only minimal assumptions about the physicality of the mass distribution, including no assumptions about LTM.

As the strongest known gravitational lens on our sky for some time, A1689 has provided us with an excellent laboratory. It was the first cluster to have its mass measured via both analyses of WL (Tyson et al. 1990) and magnification of the background galaxy population (Taylor et al. 1998). Yet before A1689 was observed with ACS, no multiple images had been identified in the field except for two fold arcs, our 8ab and 13abc (Miralda-Escude & Babul 1995). These arcs were sufficient for a rudimentary SL analysis to be performed yielding an Einstein radius of $R_E \approx 45''$, the largest of any known lens at the time.

With such a large Einstein radius, the ACS GTO team devoted 20 orbits to imaging the cluster, confident that it would reveal many highly magnified background galaxies and multiple image systems.

The observations (obtained in 2002 June) delivered, and the 100+ multiple images still far surpass any other gravitational lens. To date, other clusters observed to the same depth have yielded far fewer multiple images: 53, 35, and 33 from A1703, A2218, and CL0024, respectively (Richard et al. 2009; Elíasdóttir et al. 2007; Zitrin et al. 2009b). A1689's many SL constraints allow for detailed mass modeling, spawning many publications, and helping to make A1689 one of the best-studied galaxy clusters.

One result that stands out from both lensing and X-ray analyses of A1689 is that its mass appears to be more centrally concentrated than predicted by cold dark matter (CDM) simulations of structure formation. Simulated dark matter halos have mass profiles which are generally well described by Navarro–Frenk–White (NFW; Navarro et al. 1996) or Einasto/Sérsic (Navarro et al. 2004) profiles (e.g., Navarro et al. 2010). More massive clusters (such as A1689) finished forming later when the universe was less dense overall, and thus are found (at least in simulations) to be less centrally concentrated. Yet where A1689 is expected (Duffy et al. 2008) to have an NFW concentration of $c_{200} = 3.0^{+1.3}_{-0.9}$ ($c_{\rm vir} = 3.9^{+1.6}_{-1.1}$), it has been shown observationally (Table 2) to have a much higher concentration $c_{200} \sim 7$–11 ($c_{\rm vir} \sim 8$–12).[8]

As one of the strongest lenses on our sky, we might expect A1689's concentration to be on the high side. However, even accounting for triaxiality (Oguri et al. 2005; Corless et al. 2009) and selection (lensing) bias (Hennawi et al. 2007; Oguri & Blandford 2009; Meneghetti et al. 2010a), A1689's high concentration still seems extremely unlikely (Broadhurst & Barkana 2008).

Lensing analyses of larger samples of clusters seem to support the idea that clusters may have higher concentrations (Broadhurst et al. 2008; Oguri et al. 2009; Sereno et al. 2010)

---

6 Strong Lensing Analysis Package.
7 While the observed image positions do have (small) observational uncertainties of a pixel ($0\overset{''}{.}05$) or so, our solutions do perfectly fit the data as input.

8 Morandi et al. (2010) claim to account for A1689's high concentration (along with the discrepancy between lensing and X-ray masses) by fitting an three-dimensional ellipsoidal gNFW profile (with variable central slope) simultaneously to the SL, WL, and X-ray data. While the method is impressive, simulated clusters have yet to be analyzed in the same way (they are normally fit to spherical NFW profiles), so it is unclear that a direct comparison can be made.

Table 2
Published Concentration Measurements of A1689

c_{200}[a]	Alias	Paper	Constraints[b]
6		Clowe & Schneider (2001)	WL
4.7		King et al. (2002b)	WL
5.7		King et al. (2002a)	WL (infrared)
7.9		Clowe (2003)	WL
$3.5^{+0.5}_{-0.3}$		Bardeau et al. (2005)	WL
5.2 ± 0.3		Bardeau et al. (2007)	WL
$6.5^{+1.9}_{-1.6}$	B05	Broadhurst et al. (2005b)	SL
$10.8^{+1.2}_{-0.8}$		Broadhurst et al. (2005a)	SL + WL
$5.7^{+0.34}_{-0.5}$	Z06	Zekser et al. (2006)	SL
6 ± 0.5	H06	Halkola et al. (2006)	SL
$7.6^{+0.3}_{-0.5}$	H06	Halkola et al. (2006)	SL + WL
6.0 ± 0.6[c]	L07	Limousin et al. (2007b)	SL
7.6 ± 1.6	L07	Limousin et al. (2007b)	WL
7.6 ± 1.3	LP	This work	SL
9.2 ± 1.2		This work	SL + WL
$10.7^{+4.5}_{-2.7}$		Umetsu & Broadhurst (2008)	WL + counts
$10.1^{+0.8}_{-0.7}$		Umetsu & Broadhurst (2008)	SL + WL + counts
$12.5^{+3.9}_{-2.7}$		Umetsu et al. (2009)	WL
$9.8^{+0.7}_{-0.6}$		Umetsu et al. (2009)	SL + WL + counts
11.10		Corless et al. (2009)	WL
12.2 ± 6.7[d]		Corless et al. (2009)	WL + RE + priors
$7.7^{+1.7}_{-2.6}$		Andersson & Madejski (2004)	X-ray
5.6		Riemer-Sørensen et al. (2009)	X-ray
$5.3^{+1.3}_{-1.2}$		Peng et al. (2009)	X-ray (non-parametric)
6.6 ± 0.4		Peng et al. (2009)	X-ray (parametric)
10.9 ± 3.5		EFusco-Femiano et al. (2009)	X-ray
$9.7^{+0.7}_{-0.8}$		Lemze et al. (2008)	SL + WL + X-ray
> 10.4		Lemze et al. (2009)	SL + WL + counts + X-ray + dynamical
4.58 ± 0.34[e]		Morandi et al. (2010)	SL + WL + X-ray

Notes. For previous compilations of concentrations derived for A1689, see Comerford & Natarajan (2007, their Table A1), Limousin et al. (2007b, their Table 4), Umetsu & Broadhurst (2008, their Table 5), and Corless et al. (2009, their Table 4).
[a] Fits to spherical NFW profiles unless indicated otherwise. Concentrations assuming an overdensity of 200 (converted from quoted values if necessary).
[b] SL: strong lensing; WL: weak lensing; RE: Einstein radius; counts: magnification depletion; X-ray; dynamical: cluster galaxy velocity measurements.
[c] 3σ uncertainties.
[d] Includes uncertainties due to halo triaxiality.
[e] Fit to ellipsoidal gNFW profile (with variable central slope).

and larger Einstein radii (Broadhurst & Barkana 2008; Richard et al. 2010; Zitrin et al. 2010a) than simulated clusters. However, only a small lensing-biased sample of these has been studied in sufficient detail. We note that joint SL + WL fitting is required to constrain mass profiles well and concentrations to ~10% according to simulations (Meneghetti et al. 2010b). The addition of X-ray, SZ, and/or velocity dispersion data can constrain the mass profiles further still (Sand et al. 2008; Newman et al. 2009; Lemze et al. 2009).

More conclusive results are expected from the "CLASH"[9] Treasury Project, a large (524 orbit) *Hubble Space Telescope* (*HST*) Multi-Cycle Treasury program (PI: Postman) to observe 25 X-ray-selected galaxy clusters at $0.18 < z < 0.9$, each to a depth of 20 orbits, or the depth of the ACS GTO images of five clusters including A1689. Combined with Subaru images and other data, these observations should yield conclusive results (see Section 7).

Might baryons, lacking from the simulations discussed above, be responsible for higher mass concentrations in nature (e.g.,

Barkana & Loeb 2009)? Recent hydrodynamical simulations (Duffy et al. 2010; Mead et al. 2010) show this is unlikely. Baryons appear to increase cluster concentrations only modestly at best (~10%), though they more likely decrease concentrations slightly (as found when strong active galactic nucleus (AGN) feedback is included in the simulations).

If real clusters in fact have higher concentrations than simulated clusters, this could imply that clusters formed earlier in nature than in simulations. One mechanism to explain such early growth is a small but non-negligible amount of dark energy in the early universe, say $\Omega_{DE} \sim 0.10$ at $z = 6$ (Fedeli & Bartelmann 2007; Sadeh & Rephaeli 2008; Francis et al. 2009; Grossi & Springel 2009). The additional dark energy actually *suppresses* formation of structure, but this means that structures must have formed earlier to reach the abundances observed today. Perhaps high cluster concentrations along with detections of massive halos at $z > 1$ (Eisenhardt et al. 2008; Jee et al. 2009; Huang et al. 2009; Papovich et al. 2010; Schwope et al. 2010) are providing observational hints of such early dark energy (EDE).

We note that semianalytic modeling of cluster formation (in a "standard" ΛCDM universe) suggests that high concentrations ($c \sim 10$) may be fairly common in nature and that cluster mass

Q2

Table 3
A1689 Observations

Telescope/Camera/Detector	Filter	FWHM	Area	Magnitude Limit[a]
ACS/WFC	g'	$0\rlap{.}''11$	$11.8\square'$	27.24
ACS/WFC	r'	$0\rlap{.}''10$	$11.8\square'$	27.00
ACS/WFC	i'	$0\rlap{.}''10$	$11.8\square'$	26.92
ACS/WFC	z'	$0\rlap{.}''11$	$11.8\square'$	26.50
DuPont Telescope @ Las Campanas	U Johnson	$0\rlap{.}''93$	$72.3\square'$	$\cdots$
Nordic Optical Telescope (NOT) @ La Palma	B NOT	$1\rlap{.}''13$	$41.0\square'$	$\cdots$
Keck II/LRIS	V LRIS	$0\rlap{.}''81$	$80.1\square'$	27.17
Keck II/LRIS	R LRIS	$0\rlap{.}''74$	$93.1\square'$	26.96
Keck II/LRIS	I LRIS	$0\rlap{.}''68$	$88.7\square'$	26.41
ESO NTT/SOFI	J SOFI	$0\rlap{.}''87$	$50.4\square'$	25.12
ESO NTT/SOFI	H Johnson	$0\rlap{.}''99$	$44.9\square'$	24.22
ESO NTT/SOFI	K_s SOFI	$0\rlap{.}''82$	$50.4\square'$	24.06

Note. [a] AB, 5σ within a $0\rlap{.}''8$ diameter aperture (except for ACS, which is 10σ, $0\rlap{.}''2$ diameter aperture).

profiles may differ slightly from the NFW profiles found in simulations (Lapi & Cavaliere 2009).

In this paper, we focus on presenting our revised multiple image identifications, our mass model, and mass profile fits to SL and WL data, including measurements of the mass–concentration. In future work, we will take greater advantage of our method's main strength: the ability to map substructure without assuming LTM.

Our outline is as follows. The observations, object detections, 12-band photometry, and photometric redshifts are described in Section 2. In Section 3, we discuss the observed multiple image systems, including our additions and revisions to those previously identified. In Section 4, we review our LensPerfect method and discuss some minor improvements we have made to it. Our mass maps are presented in Section 5 and the mass profile is analyzed in Section 6. We discuss substructure and future work in Section 7 and summarize in Section 8.

We use a concordance cosmology of $(\Omega_m, \Omega_\Lambda, h) = (0.3, 0.7, 0.7)$. In this cosmology, $1'' \approx 3.11$ kpc h_{70}^{-1} at A1689's redshift (measured by Frye et al. 2007) of $z = 0.187$. Though not always explicitly noted, distances and masses are given in units of h_{70}^{-1}, where $H_0 = 70\,h_{70}$ km s^{-1} Mpc^{-1} and $h = 0.7\,h_{70}$. These values would be 30% lower if quoted in units of h^{-1} instead.

2. PHOTOMETRY AND PHOTOMETRIC REDSHIFTS

Multiband observations provide color information which is absolutely essential to the identification of multiple images. They also allow us to obtain photometric redshift estimates where spectroscopic redshifts are unavailable. Redshifts are essential to the mass model, as lensing deflections scale with redshift.

A1689 is among the best-studied galaxy clusters, having been imaged in 12 broadband filters from the near-ultraviolet to near-infrared. This allows us to obtain robust photometric redshifts, as we describe below. By carefully modeling and subtracting the light from most of the cluster galaxies, we recover many faint objects lost in their glare, including demagnified central images which allow us to constrain the mass model at small radius.

Much of the analysis described in this section was performed for and utilized by B05.

2.1. Observations

A1689 (R.A. = $13^h11^m30\rlap{.}^s13$, decl. = $-01°20'16\rlap{.}''2$ [J2000]) has been observed in four filters ($g'r'i'z'$) with ACS and eight

more ($UBVRIJHK_s$) from the ground. Details are provided in Table 3.

The ACS observations are among the deepest to date for any galaxy cluster. In 2002 June, 20 orbits of *HST* ACS GTO time were used to obtain deep exposures in the g_{475}, r_{625}, i_{775}, and z_{850} passbands (4, 4, 5, and 7 orbits, respectively). More details about the ACS observations can be found in B05.

2.2. Galaxy Detection

Objects were detected in an ACS $g' + r' + i' + z'$ detection image (with each image normalized to its background rms) using SExtractor (Bertin & Arnouts 1996). Our first detection was conservative (DEBLEND_MINAREA = 5, DETECT_THRESH = 5) and specially designed to properly deblend the cluster galaxies (DEBLEND_NTHRESH = 32, DEBLEND_MINCONT = 0.005).

Cluster members were identified by their colors, and their light was carefully modeled and subtracted from the images (K. C. Zekser et al., in preparation). This aids greatly in the detection of background objects, especially demagnified multiple images located behind the main cluster galaxies. These central images provide valuable constraints to our lensing mass model. This galaxy subtraction also improves our photometry measurements and thus photometric redshifts for any background galaxy images strongly bathed in the light of a nearby cluster galaxy.

We are now able to rerun SExtractor and detect many galaxies revealed by the subtraction of the cluster galaxies. But the detection and object segmentation (the art of assigning each pixel to a given object) are still not perfect. We inspect all of the object segmentations and edit them "by hand" where necessary. We also add a few multiple images which are predicted by our mass model and are visible in the images but managed to escape detection, either due to a bright neighbor or otherwise. Using the SExSeg package (Coe et al. 2006), we are able to force our revised object definitions into SExtractor for photometric analysis.

2.3. Photometry

With observations obtained from a wide range of telescopes, both from space and from the ground, care must be taken to obtain robust point-spread function (PSF)-corrected aperture-matched photometry. This proves especially crucial for the faint lensed background galaxies we are most interested in. Thus, we use the software package ColorPro, which we developed and applied previously to obtain robust photometry of galaxies in

Q3

the UDF (Coe et al. 2006). As in our UDF analysis, we also recalibrate the photometric zero points of several of our images. This procedure is described below.

2.4. Photometric Redshifts

Photometric redshifts were obtained for the objects in our A1689 catalog using an updated version 1.99.2 of the Bayesian Photometric Redshift software BPZ (Benítez 2000). This version features the recalibrated CWW + SB spectral energy distribution (SED) templates introduced in Benítez et al. (2004) plus the two younger starburst templates added in Coe et al. (2006).

In our UDF analysis (Coe et al. 2006), we reported a photometric redshift accuracy of $\Delta z = 0.04(1 + z_{spec})$. Here we expect to achieve similar, or perhaps slightly worse, precision. The A1689 exposures are not as deep as the UDF, although in regions of high magnification ($\mu \gtrsim 6; \Delta m \gtrsim 2$), we can actually detect fainter galaxies than possible in the UDF. The images are very crowded with cluster galaxies whose light may contaminate that of neighbors (despite our best efforts to model and subtract this light) affecting the photometry and thus photometric redshifts.

A1689 has been the target of several spectroscopic redshift campaigns, including Teague et al. (1990), Fort et al. (1997), Balogh et al. (2002), Duc et al. (2002), Frye et al. (2002), and Frye et al. (2007). Of the spectroscopic redshifts published in these works, 113 lie within the ACS field of view (FOV). These are presented in Table 4. Of these objects, three are stars, another (no. 172) is half outside the ACS FOV, and for another (no. 194) it was unclear which object was being referenced by the published coordinates. What remain are 108 galaxies. In our first attempt to obtain photometric redshifts for these galaxies, it was clear that our SED templates provided a poor fit for the observed U and B magnitudes.

To reveal flux miscalibrations in any of the filters, we apply techniques similar to that used in our study of the UDF (Coe et al. 2006). We select cluster ellipticals based on their spectroscopic redshift, BPZ spectral type fit, and visual confirmation in the ACS images. We then use BPZ to fit SEDs to the photometry of these objects, fixing the redshifts at the spectroscopically determined values. We find the following offsets between the observed and predicted magnitudes: $V -0.08$, $R -0.10$, $I -0.00$, $J -0.08$, $H -0.06$, $K_s +0.01$, $g' -0.15$, $r' +0.03$, $i' -0.04$, and z' +0.02. We subtract these biases from our measured magnitudes. Our U- and B-band images did not arrive well calibrated, so we used this procedure to calibrate them as well.

Given our recalibrated fluxes, we rerun BPZ on all our galaxies without constraining the redshifts to the correct values as above. We measure of goodness of fit χ^2_{mod} between observed and model fluxes with some uncertainty assigned to the model fluxes (see Coe et al. 2006). An example of an excellent ($\chi^2_{mod} = 0.03$) and correct ($\Delta z = 0.01$) SED fit to a cluster elliptical obtained with recalibrated fluxes is shown in Figure 1. Of the 108 galaxies with spectroscopic redshifts in the ACS FOV, we obtained good SED fits ($\chi^2_{mod} < 1$) for 89. For these 89 objects, our Bayesian photometric redshifts agree with the spectroscopic redshifts to within $\Delta z = 0.07(1 + z_{spec})$ (see Figure 2). And if we recursively remove outliers with more than three times this deviation (as in Coe et al. 2006), then two galaxies are pruned and the remaining 87 agree to within $\Delta z = 0.06(1 + z_{spec})$. The two outliers are hardly catastrophic, having $\Delta z = 0.30(1 + z_{spec})$ and $\Delta z = 0.21(1 + z_{spec})$.

Finally, we obtain photometry and photometric redshifts for our multiple images. The results are given in Table 5. For each

Table 4
Spectroscopic Redshifts of Galaxies within the ACS Field of View of A1689 Used for Our Photometric Redshift Tests

ID	R.A. and Decl. (J2000)[a]		Survey[b]	z_{spec}
451	13:11:32.606	−1:19:22.920	Miekse	0.0000
366	13:11:24.802	−1:20:23.070	Frye	0.0000
374	13:11:26.919	−1:20:00.650	Frye	0.0000
216	13:11:28.344	−1:18:32.380	MOS	0.0130
213	13:11:27.224	−1:20:10.180	MOS	0.0862
220	13:11:33.034	−1:21:24.780	MOS	0.1430
74	13:11:25.382	−1:20:17.140	Balogh*	0.1660
7	13:11:32.089	−1:19:36.600	Balogh*	0.1690
127	13:11:28.194	−1:20:43.680	MOS*	0.1712
194	13:11:30.934	−1:20:30.680	Teague*	0.1739
387	13:11:30.508	−1:19:34.670	Frye	0.1740
378	13:11:27.851	−1:20:07.650	Frye	0.1750
192	13:11:30.234	−1:20:27.680	Teague*	0.1750
124	13:11:27.894	−1:21:36.880	MOS*	0.1752
184	13:11:26.884	−1:19:37.180	Teague*	0.1754
43	13:11:37.981	−1:20:09.780	Balogh*	0.1760
108	13:11:24.284	−1:21:14.480	MOS*	0.1766
198	13:11:32.094	−1:21:38.380	Teague*	0.1770
4	13:11:28.344	−1:19:58.300	Balogh*	0.1775
154	13:11:32.464	−1:22:18.280	MOS*	0.1794
112	13:11:25.104	−1:19:31.380	MOS*	0.1797
383	13:11:28.886	−1:20:01.940	Frye	0.1800
141	13:11:29.994	−1:20:17.580	MOS*	0.1801
152	13:11:32.104	−1:19:47.180	MOS*	0.1801
61	13:11:31.510	−1:19:24.870	Balogh*	0.1817
9	13:11:34.058	−1:21:01.990	Balogh*	0.1826
370	13:11:26.237	−1:19:56.450	Frye	0.1830
201	13:11:35.374	−1:20:43.080	Teague*	0.1835
64	13:11:29.386	−1:18:34.790	Balogh*	0.1836
172	13:11:37.834	−1:19:20.880	MOS*	0.1839
375	13:11:27.148	−1:18:48.440	Frye	0.1840
135	13:11:29.474	−1:20:28.080	MOS*	0.1842
118	13:11:27.084	−1:18:48.880	MOS*	0.1852
153	13:11:32.204	−1:22:10.980	MOS*	0.1855
188	13:11:29.074	−1:21:37.380	Teague*	0.1858
132	13:11:28.724	−1:19:02.980	MOS*	0.1859
450	13:11:32.761	−1:19:48.930	Miekse	0.1859
63	13:11:29.869	−1:20:15.230	Balogh*	0.1868
165	13:11:35.344	−1:21:33.480	MOS*	0.1870
69	13:11:28.023	−1:18:43.890	Balogh*	0.1870
110	13:11:24.434	−1:21:11.180	MOS*	0.1870
147	13:11:31.064	−1:21:27.980	MOS*	0.1872
384	13:11:29.100	−1:19:46.920	Frye	0.1880
6	13:11:31.400	−1:19:32.840	Balogh*	0.1884
196	13:11:31.074	−1:20:52.780	Teague*	0.1885
419	13:11:38.051	−1:19:58.250	Frye	0.1890
390	13:11:31.472	−1:21:05.940	Frye	0.1890
163	13:11:34.754	−1:20:59.480	MOS*	0.1895
189	13:11:29.114	−1:21:55.480	Teague*	0.1908
131	13:11:28.594	−1:20:26.780	MOS*	0.1909
70	13:11:26.812	−1:19:43.090	Balogh*	0.1910
146	13:11:30.564	−1:20:43.980	MOS*	0.1918
1	13:11:25.354	−1:20:37.060	Balogh*	0.1922
133	13:11:29.294	−1:19:16.980	MOS*	0.1932
187	13:11:28.994	−1:21:16.980	Teague*	0.1947
71	13:11:25.925	−1:19:51.950	Balogh*	0.1950
119	13:11:27.094	−1:21:43.080	MOS*	0.1955
12	13:11:36.616	−1:19:42.800	Balogh*	0.1960
148	13:11:31.124	−1:21:25.380	MOS*	0.1972
123	13:11:27.834	−1:21:13.080	MOS*	0.1977
115	13:11:25.974	−1:19:35.680	MOS*	0.1983
140	13:11:29.984	−1:22:07.580	MOS*	0.1985
11	13:11:35.595	−1:20:12.400	Balogh*	0.1995
128	13:11:28.324	−1:18:45.180	MOS*	0.1999
395	13:11:33.234	−1:19:17.000	Frye	0.2000

Table 4
(Continued)

ID	R.A. and Decl. (J2000)[a]		Survey[b]	z_{spec}
139	13:11:29.974	−1:20:40.480	MOS*	0.2002
158	13:11:32.704	−1:19:32.080	MOS*	0.2009
143	13:11:30.044	−1:20:42.980	MOS*	0.2012
452	13:11:29.905	−1:20:05.430	Miekse	0.2014
157	13:11:32.654	−1:19:58.980	MOS*	0.2022
2	13:11:27.109	−1:20:58.420	Balogh*	0.2147
82	13:11:23.065	−1:21:17.280	Balogh*	0.2150
3	13:11:27.681	−1:21:07.190	Balogh*	0.2158
398	13:11:33.555	−1:19:01.500	Frye	0.2440
221	13:11:33.724	−1:19:39.180	MOS	0.3100
214	13:11:27.844	−1:18:52.980	MOS	0.3840
399	13:11:33.621	−1:22:02.190	Frye	0.3870
376	13:11:27.204	−1:18:49.920	Frye	0.4800
365	13:11:24.652	−1:20:03.380	Frye	0.4810
405	13:11:35.088	−1:21:26.010	Frye	0.5840
406	13:11:35.258	−1:20:30.170	Frye	0.5870
418	13:11:37.699	−1:19:50.030	Frye	0.6250
388	13:11:30.677	−1:18:55.500	Frye	0.6760
402	13:11:34.328	−1:19:05.100	Frye	0.6760
389	13:11:30.751	−1:21:38.780	Frye	0.6910
379	13:11:28.221	−1:20:50.930	Frye	0.7030
380	13:11:28.325	−1:18:27.500	Frye	0.7100
367	13:11:24.960	−1:19:36.610	Frye	0.7220
364	13:11:24.609	−1:19:20.830	Frye	0.7570
411	13:11:36.536	−1:19:25.030	Frye	0.7900
396	13:11:33.028	−1:19:14.650	Frye	0.7900
217	13:11:28.764	−1:21:43.580	MOS	0.7900
414	13:11:37.183	−1:20:16.890	Frye	0.8130
362	13:11:24.240	−1:19:52.680	Frye	0.8570
363	13:11:24.398	−1:19:36.880	Frye	0.8950
409	13:11:36.052	−1:19:24.710	Frye	0.9160
413	13:11:37.089	−1:19:26.100	Frye	0.9240
373	13:11:26.683	−1:19:36.770	Frye	0.9590
393	13:11:32.056	−1:21:55.410	Frye	0.9590
356	13:11:22.472	−1:20:39.220	Frye	0.9600
401	13:11:34.242	−1:19:23.970	Frye	1.0510
377	13:11:27.191	−1:18:26.550	Frye	1.1120
361	13:11:24.186	−1:19:56.550	Frye	1.1550
400	13:11:33.950	−1:19:15.750	Frye	1.3620
306	13:11:33.981	−1:20:50.950	Broadhurst	1.3700
302	13:11:27.359	−1:20:54.900	Broadhurst	1.8200
301	13:11:30.294	−1:19:50.920	Broadhurst	1.8200
371	13:11:26.541	−1:19:55.700	Frye	2.5360
307	13:11:33.065	−1:20:27.450	Broadhurst	3.0410
308	13:11:26.441	−1:19:56.940	Broadhurst	3.0410
385	13:11:29.969	−1:19:14.880	Frye	3.8500
368	13:11:25.447	−1:20:51.740	Frye	4.8680
404	13:11:34.994	−1:19:51.170	Frye	5.1200

Notes.
[a] Slight modifications have been made to the previously published coordinates where necessary.
[b] Redshift surveys are Balogh et al. (2002), MOS (Duc et al. 2002), Teague et al. (1990), Broadhurst et al. (2005b), and Frye et al. (2002, 2007). Asterisks (*) indicate galaxies designated as "spectroscopically confirmed cluster members" in each survey.

Figure 1. Example of an excellent BPZ SED fit to the photometry of a cluster elliptical (no. 198), after flux recalibrations of all filters (see the text). The photometric redshift is correctly derived as $z = 0.18 \pm 0.12$ (95% confidence). The colored circles give the observed AB magnitudes with uncertainties in 12 filters, while the blue rectangles give the SED model-predicted magnitudes (with rough uncertainties) in those filters. The colors serve to distinguish the telescopes/filters: purple—Las Campanas, La Palma (UB); green—ACS ($g'r'i'z'$); orange—Keck/LRIS (VRI); red—ESO NTT/SOFI (JHK_s).
(A color version of this figure is available in the online journal.)
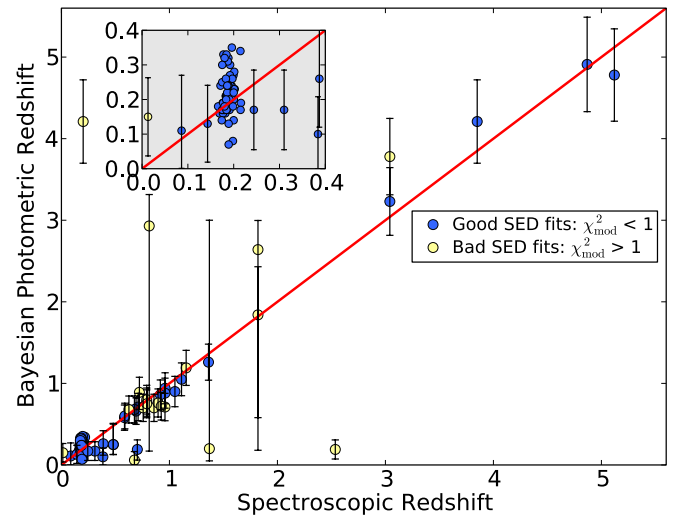
Figure 2. Bayesian photometric redshifts plotted vs. 108 spectroscopic redshifts obtained within the ACS FOV (Table 4). Good BPZ SED fits ($\chi^2_{mod} < 1$) are plotted in blue, while poorer fits to the photometry are plotted in yellow. For the 89 galaxies with good SED fits, the photometric redshifts agree with the spectroscopic values to within $\Delta z = 0.07(1 + z_{spec})$. If we recursively remove outliers with more than three times the rms deviation Δz (as in Coe et al. 2006), two galaxies are pruned and the rest agree to within $\Delta z = 0.06(1 + z_{spec})$.
(A color version of this figure is available in the online journal.)

redshift, a 95% confidence interval is quoted as well as χ^2_{mod}. Note that in B05 the BPZ prior was modified. The redshift range $z < 0.7$ was excluded and the prior allowed for observed fluxes up to 20× magnified. We have not implemented this modified prior here.

Note that these redshifts were obtained using photometry from all 12 filters. We have also obtained photometric redshifts
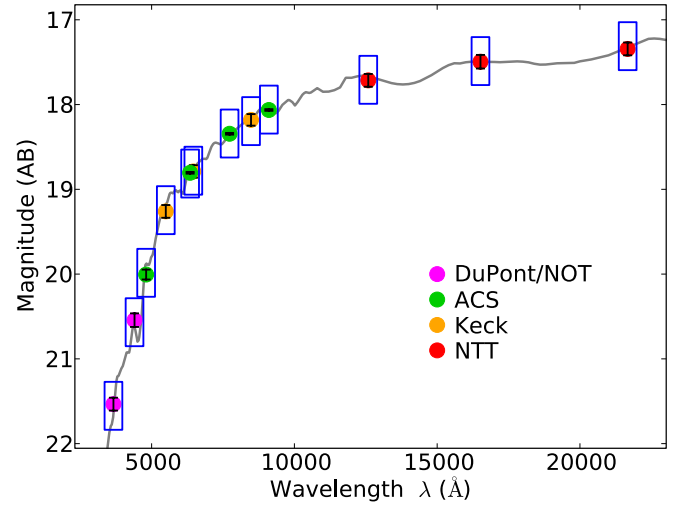
based on photometry obtained in the four ACS images with the light of cluster galaxies modeled and subtracted. We are unable to apply this galaxy subtraction in a consistent and robust manner to the ground-based images due to their significantly worse PSFs. Yet even with four filters, we obtain improved photometric redshifts for those objects whose light is significantly contaminated by nearby cluster galaxies.

Table 5
Multiple Images Produced by A1689

| ID | ID[a] | x[b] | y[b] | R.A. | Decl. | i'_{775} | Magnification[c] | | Spec./Photometric Redshift[d] | | |
	B05	(pixel)	(pixel)	(J2000.0)	(J2000.0)	(AB mag)	Final	Range	z_{spec}[e]	z_b[f]	χ^2_{mod}[g]
1a	''	2213	1055	13 11 26.452	−1 19 56.75	23.31 ± 0.01	14.2	$11.9^{+3.2}_{-2.5}$	$3.04^{2,3}$	$3.21^{+0.65}_{-0.41}$	1.1
b	''	2130	1040	13 11 26.289	−1 20 00.19	23.60 ± 0.01	42.7	$28.2^{+30.3}_{-14.6}$	(3.04)	3.88 ± 0.48	1.1
c	''	1356	2557	13 11 29.773	−1 21 07.43	24.51 ± 0.02	1.5	$1.7^{+0.3}_{-0.2}$	$3.04^{2,3}$	3.79 ± 0.47	3.5
d	''	2499	3112	13 11 33.066	−1 20 27.47	24.03 ± 0.01	2.8	$2.9^{+0.7}_{-0.6}$	(3.04)	3.76 ± 0.47	2.4
e	''	2745	2621	13 11 31.932	−1 20 05.91	24.64 ± 0.02	1.6	$1.7^{+0.2}_{-0.2}$	(3.04)	$3.17^{+0.72}_{-0.41}$	0.6
f	''	1890	2333	13 11 29.852	−1 20 38.50	24.94 ± 0.05	0.5	$0.7^{+0.3}_{-0.2}$	(3.04)	$0.51^{+2.66}_{-0.41}$	2.2
2a	''	2245	1064	13 11 26.524	−1 19 55.49	23.24 ± 0.01	6.5	$5.1^{+1.5}_{-1.2}$	2.53^3	$0.16^{+0.30}_{-0.11}$	0.3
b	''	2522	3069	13 11 32.969	−1 20 25.51	23.91 ± 0.02	6.1	$4.4^{+1.1}_{-0.9}$	(2.53)	$0.20^{+0.25}_{-0.12}$	0.5
c	''	2728	2644	13 11 31.978	−1 20 07.17	24.28 ± 0.02	2.4	$2.3^{+0.1}_{-0.1}$	(2.53)	$2.69^{+0.36}_{-2.48}$	9.8
d	''	1386	2556	13 11 29.812	−1 21 06.05	24.35 ± 0.02	1.3	$1.6^{+0.3}_{-0.2}$	2.5^4	$2.66^{+0.41}_{-2.46}$	0.9
e	''	1876	2349	13 11 29.881	−1 20 39.48	24.81 ± 0.04	0.9	$0.9^{+0.2}_{-0.2}$	(2.53)	$0.31^{+2.90}_{-0.21}$	2.0
3a	''	2372	2832	13 11 32.041	−1 20 27.27	26.10 ± 0.06	5.9	$4.9^{+0.5}_{-0.5}$	⋯	0.96 ± 0.19	4.3
b	''	2279	2921	13 11 32.178	−1 20 33.37	26.29 ± 0.05	4.7	$11.5^{+11.9}_{-5.8}$	⋯	5.22 ± 0.61	1.0
c	''	1809	2984	13 11 31.703	−1 20 55.99	27.24 ± 0.13	5.1	$4.0^{+0.9}_{-0.7}$	⋯	$0.81^{+4.32}_{-0.35}$	3.7
4a	''	1844	3124	13 11 32.175	−1 20 57.37	24.17 ± 0.02	10.7	$4.9^{+2.5}_{-1.7}$	1.1^4	$0.79^{+0.47}_{-0.18}$	0.1
b	''	1369	2801	13 11 30.528	−1 21 12.02	23.53 ± 0.01	15.9	$15.7^{+8.4}_{-5.5}$	(1.1)	$1.02^{+0.53}_{-0.20}$	1.9
c	''	2553	2322	13 11 30.758	−1 20 08.25	25.02 ± 0.03	6.7	$5.1^{+1.4}_{-1.1}$	(1.1)	$1.06^{+0.20}_{-0.34}$	0.8
d	''	1492	1338	13 11 26.285	−1 20 35.40	24.61 ± 0.02	15.9	$17.2^{+27.6}_{-10.6}$	(1.1)	$0.78^{+0.51}_{-0.17}$	0.8
e	''	2052	2252	13 11 29.837	−1 20 29.45	27.17 ± 0.32	0.5	$0.6^{+0.1}_{-0.1}$	(1.1)	$0.68^{+2.84}_{-0.49}$	0.9
5a	''	1606	2205	13 11 29.064	−1 20 48.64	24.29 ± 0.03	72.2	$10.5^{+18.3}_{-6.7}$	2.6^4	$2.91^{+0.38}_{-0.48}$	0.0
b	''	1706	2211	13 11 29.224	−1 20 44.24	24.68 ± 0.04	11.5	$13.2^{+19.6}_{-7.9}$	(2.6)	$0.25^{+2.91}_{-0.14}$	1.7
c	''	2751	3343	13 11 34.120	−1 20 20.96	25.10 ± 0.03	9.0	$3.9^{+2.8}_{-1.6}$	2.6^4	3.00 ± 0.39	1.2
6a	''	3097	2066	13 11 30.755	−1 19 38.19	23.52 ± 0.02	8.2	$7.5^{+1.3}_{-1.1}$	1.1^4	1.17 ± 0.21	0.0
b	''	2811	3058	13 11 33.345	−1 20 12.20	23.62 ± 0.02	5.1	$5.3^{+1.2}_{-1.0}$	1.1^4	1.36 ± 0.23	0.7
c	''	3055	2744	13 11 32.742	−1 19 54.49	22.13 ± 0.01	16.2	$23.9^{+16.2}_{-9.7}$	(1.1)	0.98 ± 0.19	1.5
d	''	2943	2709	13 11 32.478	−1 19 58.81	21.83 ± 0.00	23.9	$17.8^{+5.9}_{-4.4}$	(1.1)	$0.53^{+0.25}_{-0.15}$	4.2
7a	''	1087	1250	13 11 25.446	−1 20 51.87	23.29 ± 0.01	243.0	$6.8^{+19.9}_{-5.1}$	4.87^1	4.93 ± 0.58	0.0
b	''	2439	2349	13 11 30.678	−1 20 13.99	24.13 ± 0.01	4.1	$3.0^{+1.2}_{-0.8}$	4.8^4	4.86 ± 0.57	1.8
8a	''	1974	3105	13 11 32.302	−1 20 51.09	22.01 ± 0.01	22.7	$8.6^{+6.2}_{-3.6}$	⋯	$0.15^{+0.31}_{-0.11}$	0.3
b	''	1596	2984	13 11 31.402	−1 21 05.63	21.59 ± 0.01	22.7	$33.5^{+29.2}_{-15.6}$	⋯	$0.48^{+0.15}_{-0.39}$	1.4
c	''	2541	2572	13 11 31.495	−1 20 14.10	25.55 ± 0.05	5.5	$7.9^{+6.2}_{-3.5}$	⋯	$0.22^{+2.86}_{-0.12}$	4.4
d	''	1674	1001	13 11 25.526	−1 20 20.01	22.28 ± 0.01	24.8	$21.5^{+25.8}_{-11.7}$	⋯	0.50 ± 0.15	1.2
9a	''	2850	2032	13 11 30.303	−1 19 48.65	25.66 ± 0.04	14.0	$14.6^{+3.1}_{-2.6}$	⋯	4.80 ± 0.57	4.2
b	''	2141	3430	13 11 33.519	−1 20 50.42	27.27 ± 0.09	2.9	$3.4^{+1.3}_{-0.9}$	⋯	$0.79^{+4.33}_{-0.18}$	1.0
c	''	1072	2347	13 11 28.737	−1 21 15.83	25.56 ± 0.04	22.5	$5.0^{+4.1}_{-2.2}$	⋯	$0.76^{+3.94}_{-0.17}$	4.0
d	''	1645	1264	13 11 26.279	−1 20 26.90	26.94 ± 0.07	4.4	$3.3^{+0.6}_{-0.5}$	⋯	$4.95^{+0.58}_{-4.23}$	1.4
10a	''	2189	3560	13 11 33.980	−1 20 51.01	23.01 ± 0.01	2.3	$3.1^{+1.4}_{-1.0}$	1.83^4	$0.26^{+2.32}_{-0.21}$	0.5
b	''	2130	1625	13 11 28.055	−1 20 12.61	22.66 ± 0.01	2.7	$4.7^{+3.1}_{-1.9}$	(1.83)	$0.12^{+0.60}_{-0.11}$	0.6
c	''	2012	2098	13 11 29.316	−1 20 27.99	23.61 ± 0.02	0.4	$0.4^{+0.1}_{-0.1}$	(1.83)	$0.56^{+0.15}_{-0.37}$	6.7
11a	''	1824	3522	13 11 33.349	−1 21 06.73	23.79 ± 0.02	3.9	$2.4^{+0.4}_{-0.4}$	2.5^4	2.89 ± 0.38	0.1
b	''	2462	1801	13 11 29.056	−1 20 01.31	23.40 ± 0.01	8.9	$6.1^{+1.4}_{-1.2}$	(2.5)	$2.82^{+0.37}_{-2.52}$	0.1
c	''	2062	2135	13 11 29.498	−1 20 26.51	23.73 ± 0.01	0.2	$0.2^{+0.0}_{-0.0}$	(2.5)	$0.53^{+0.20}_{-0.22}$	2.3
12b	''	1275	1796	13 11 27.361	−1 20 54.94	24.18 ± 0.02	49.3	$20.5^{+25.0}_{-11.3}$	$1.83^{2,4}$	$0.60^{+2.01}_{-0.45}$	0.6
c	''	1311	1730	13 11 27.213	−1 20 51.91	23.84 ± 0.01	28.6	$18.0^{+8.2}_{-5.6}$	(1.83)	0.60 ± 0.16	0.4
f	⋯	1602	1547	13 11 27.072	−1 20 34.86	25.40 ± 0.07	7.5	$6.7^{+0.4}_{-0.4}$	(1.83)	$2.10^{+0.48}_{-0.60}$	9.2
g	⋯	2197	1563	13 11 27.963	−1 20 08.26	22.83 ± 0.00	3.2	$2.4^{+0.6}_{-0.5}$	(1.83)	$1.64^{+0.26}_{-1.23}$	3.5
h	⋯	2190	3463	13 11 33.688	−1 20 48.91	28.08 ± 0.15	5.0	$3.9^{+0.9}_{-0.7}$	(1.83)	$2.00^{+1.26}_{-1.78}$	7.1
i	⋯	2224	1497	13 11 27.802	−1 20 05.64	23.81 ± 0.01	6.8	$4.1^{+2.1}_{-1.4}$	(1.83)	$0.19^{+0.37}_{-0.12}$	6.4
13a	''	3610	2512	13 11 32.828	−1 19 24.44	23.63 ± 0.02	14.1	$23.2^{+9.6}_{-6.8}$	⋯	1.03 ± 0.20	1.5
b	''	3605	2567	13 11 32.986	−1 19 25.83	23.76 ± 0.02	64.3	$38.1^{+55.6}_{-22.6}$	⋯	0.37 ± 0.13	0.9
c	''	3559	2725	13 11 33.398	−1 19 31.27	23.60 ± 0.02	24.9	$20.1^{+17.3}_{-9.3}$	⋯	$1.16^{+0.33}_{-0.21}$	1.6
14a	''	639	2648	13 11 29.033	−1 21 41.82	25.14 ± 0.04	70.5	$33.9^{+75.6}_{-23.4}$	3.4^4	$0.55^{+2.66}_{-0.40}$	115.6
b	''	677	2772	13 11 29.461	−1 21 42.73	25.70 ± 0.05	195.9	$49.9^{+61.4}_{-27.5}$	(3.4)	$3.37^{+0.44}_{-0.43}$	3.7
15a	15.2	1356	2557	13 11 29.773	−1 21 07.43	25.51 ± 0.04	2.8	$3.3^{+1.0}_{-0.8}$	1.8^4	$1.91^{+0.45}_{-1.63}$	2.5
b	15.1	2213	1055	13 11 26.452	−1 19 56.75	24.72 ± 0.04	7.9	$9.1^{+3.0}_{-2.2}$	(1.8)	$1.73^{+0.84}_{-1.60}$	2.9
c	''	2009	2074	13 11 29.239	−1 20 27.62	25.62 ± 0.06	0.7	$0.9^{+0.2}_{-0.1}$	(1.8)	$0.43^{+1.96}_{-0.24}$	1.1

Table 5
(Continued)

ID	ID[a]	x[b]	y[b]	R.A.	Decl.	i'_{775}	Magnification[c]		Spec./Photometric Redshift[d]		
	B05	(pixel)	(pixel)	(J2000.0)	(J2000.0)	(AB mag)	Final	Range	z_{spec}[e]	z_b[f]	χ^2_{mod}[g]
16a	”	1892	1715	13 11 27.990	−1 20 25.29	23.31 ± 0.01	18.9	$18.0^{+4.3}_{-3.5}$	⋯	$1.89^{+0.44}_{-0.28}$	0.7
b	”	1950	1991	13 11 28.905	−1 20 28.53	24.54 ± 0.05	5.6	$4.1^{+1.4}_{-1.0}$	⋯	$0.87^{+1.52}_{-0.71}$	4.8
c	”	2326	3635	13 11 34.400	−1 20 46.40	24.99 ± 0.03	3.6	$2.2^{+0.8}_{-0.6}$	⋯	$0.25^{+2.72}_{-0.12}$	1.0
17a	”	2240	2437	13 11 30.662	−1 20 24.87	24.13 ± 0.02	2.8	$3.1^{+0.4}_{-0.4}$	(2.6)	$2.72^{+0.36}_{-0.37}$	0.9
b	”	2152	2389	13 11 30.392	−1 20 27.83	23.08 ± 0.01	1.5	$1.6^{+0.2}_{-0.2}$	(2.6)	$0.40^{+0.14}_{-0.25}$	2.9
c	”	1209	1038	13 11 24.979	−1 20 41.84	24.45 ± 0.02	2.0	$1.7^{+0.3}_{-0.2}$	2.6^4	2.69 ± 0.36	7.2
18a	18.2	2499	3112	13 11 33.066	−1 20 27.47	24.77 ± 0.02	3.8	$4.4^{+1.5}_{-1.1}$	1.8^4	$0.16^{+0.34}_{-0.11}$	1.9
b	18.1	2130	1040	13 11 26.289	−1 20 00.19	24.71 ± 0.03	2.8	$3.9^{+1.3}_{-1.0}$	(1.8)	$0.60^{+2.30}_{-0.46}$	4.1
c	”	2029	2106	13 11 29.364	−1 20 27.39	25.44 ± 0.05	0.2	$0.3^{+0.1}_{-0.1}$	(1.8)	$0.69^{+3.52}_{-0.21}$	12.3
19a	”	2404	2682	13 11 31.634	−1 20 22.64	24.42 ± 0.03	10.9	$29.0^{+66.2}_{-20.1}$	(2.6)	$0.20^{+2.43}_{-0.12}$	4.4
b	”	1637	924	13 11 25.241	−1 20 20.05	24.67 ± 0.03	32.3	$18.4^{+15.7}_{-8.5}$	(2.6)	$0.20^{+3.17}_{-0.12}$	0.8
c	”	1780	3082	13 11 31.958	−1 20 59.38	23.47 ± 0.01	13.2	$19.9^{+21.1}_{-10.2}$	(2.6)	$0.21^{+0.12}_{-0.14}$	1.4
d	”	1825	3088	13 11 32.040	−1 20 57.47	23.84 ± 0.02	25.5	$24.9^{+15.7}_{-9.6}$	2.6^4	0.15 ± 0.11	4.3
21a	”	1907	2714	13 11 31.027	−1 20 45.82	24.47 ± 0.03	3.4	$5.7^{+5.1}_{-2.7}$	⋯	$1.76^{+0.52}_{-1.52}$	0.5
b	”	1897	2650	13 11 30.819	−1 20 44.91	23.67 ± 0.01	2.5	$4.8^{+6.0}_{-2.7}$	⋯	$0.58^{+0.16}_{-0.29}$	2.1
c	”	1797	852	13 11 25.250	−1 20 11.28	25.34 ± 0.04	1.5	$2.1^{+0.4}_{-0.4}$	⋯	1.78 ± 0.27	7.5
22a	”	2407	2038	13 11 29.694	−1 20 08.84	23.68 ± 0.01	3.9	$3.3^{+0.9}_{-0.7}$	1.7^4	$0.07^{+0.38}_{-0.07}$	0.6
b	”	2127	2144	13 11 29.617	−1 20 23.76	24.18 ± 0.04	0.6	$0.5^{+0.2}_{-0.1}$	(1.7)	$1.73^{+0.27}_{-0.30}$	4.5
c	”	1539	3348	13 11 32.420	−1 21 15.94	23.19 ± 0.01	4.5	$3.5^{+1.1}_{-0.9}$	(1.7)	$0.07^{+0.36}_{-0.07}$	0.6
23a	”	2364	2005	13 11 29.533	−1 20 10.08	24.64 ± 0.02	4.2	$4.0^{+4.0}_{-2.0}$	⋯	$0.09^{+0.51}_{-0.09}$	1.3
b	”	2134	2121	13 11 29.558	−1 20 22.96	24.89 ± 0.05	0.5	$0.5^{+0.2}_{-0.1}$	⋯	$0.44^{+1.78}_{-0.32}$	1.5
c	”	1582	3408	13 11 32.662	−1 21 15.26	24.54 ± 0.02	3.1	$3.9^{+0.7}_{-0.6}$	⋯	$0.58^{+1.99}_{-0.15}$	1.3
24a	”	1485	2304	13 11 29.192	−1 20 56.22	25.07 ± 0.05	26.9	$6.3^{+7.9}_{-3.5}$	(2.6)	$0.34^{+2.68}_{-0.14}$	0.9
b	”	3039	2525	13 11 32.059	−1 19 50.56	23.81 ± 0.02	6.3	$5.4^{+2.2}_{-1.6}$	(2.6)	3.63 ± 0.45	2.5
c	”	3110	1906	13 11 30.290	−1 19 34.21	24.08 ± 0.02	6.3	$5.6^{+2.3}_{-1.6}$	2.6^4	$0.22^{+2.86}_{-0.16}$	1.2
d	”	2719	3225	13 11 33.719	−1 20 19.91	24.42 ± 0.02	3.6	$2.9^{+1.5}_{-1.0}$	(2.6)	2.94 ± 0.39	0.1
26a	”	1396	1008	13 11 25.153	−1 20 32.74	24.88 ± 0.02	14.2	$11.8^{+5.8}_{-3.9}$	⋯	1.31 ± 0.23	0.1
b	”	2317	2621	13 11 31.326	−1 20 25.28	25.33 ± 0.03	12.3	$8.0^{+2.4}_{-1.8}$	⋯	0.92 ± 0.19	3.5
c	”	2046	2389	13 11 30.242	−1 20 32.63	26.53 ± 0.20	29.9	$54.1^{+105.4}_{-35.8}$	⋯	$0.93^{+2.70}_{-0.70}$	8.1
27a	”	1391	1017	13 11 25.173	−1 20 33.16	24.98 ± 0.02	9.0	$7.8^{+2.7}_{-2.0}$	⋯	$1.08^{+0.20}_{-0.90}$	1.2
b	”	2334	2627	13 11 31.369	−1 20 24.64	25.00 ± 0.03	8.2	$7.6^{+0.6}_{-0.6}$	⋯	$1.11^{+0.21}_{-0.35}$	2.6
c	”	2034	2378	13 11 30.192	−1 20 32.94	27.04 ± 0.22	48.3	$18.1^{+21.9}_{-9.9}$	⋯	$1.12^{+2.07}_{-0.85}$	1.0
28a	”	2193	1677	13 11 28.301	−1 20 10.86	26.72 ± 0.09	4.6	$5.1^{+1.3}_{-1.0}$	⋯	$5.13^{+0.60}_{-4.36}$	1.2
b	”	2062	3713	13 11 34.262	−1 21 00.01	25.42 ± 0.04	6.2	$6.1^{+2.4}_{-1.7}$	⋯	0.72 ± 0.17	6.8
c	⋯	2034	2080	13 11 29.293	−1 20 26.61	25.61 ± 0.07	0.3	$0.4^{+0.1}_{-0.1}$	⋯	$0.80^{+0.40}_{-0.28}$	0.7
29a	”	1456	2329	13 11 29.226	−1 20 58.06	25.81 ± 0.06	129.6	$9.6^{+17.4}_{-6.2}$	(2.5)	$2.61^{+0.38}_{-2.47}$	1.8
b	”	3076	1833	13 11 30.022	−1 19 34.20	24.87 ± 0.04	45.9	$11.3^{+9.0}_{-5.0}$	(2.5)	3.58 ± 0.45	0.7
c	”	3012	2577	13 11 32.177	−1 19 52.89	25.17 ± 0.07	47.6	$11.0^{+13.2}_{-6.0}$	(2.5)	3.61 ± 0.45	1.6
d	”	2694	3206	13 11 33.626	−1 20 20.64	25.39 ± 0.04	5.6	$4.0^{+3.5}_{-1.9}$	2.5^4	3.21 ± 0.41	0.9
30a	”	3642	2362	13 11 32.420	−1 19 19.80	25.94 ± 0.05	21.9	$10.7^{+4.7}_{-3.3}$	(3.0)	$3.36^{+0.46}_{-3.00}$	1.1
b	”	3626	2623	13 11 33.185	−1 19 26.07	26.03 ± 0.05	43.3	$23.4^{+39.2}_{-14.7}$	(3.0)	$3.28^{+0.42}_{-3.09}$	1.1
c	”	3566	2809	13 11 33.662	−1 19 32.73	25.81 ± 0.05	6.0	$4.2^{+2.2}_{-1.4}$	3.0^4	$3.05^{+0.70}_{-0.40}$	2.4
31a	12.1	1890	2333	13 11 29.852	−1 20 38.50	23.98 ± 0.02	31.8	$22.3^{+16.0}_{-9.3}$	$1.83^{2,4}$	$0.70^{+0.21}_{-0.17}$	0.7
b	HL	2219	3312	13 11 33.274	−1 20 44.39	25.37 ± 0.04	3.3	$3.4^{+0.4}_{-0.4}$	(1.83)	$2.00^{+0.35}_{-1.82}$	1.9
c	12.4	2245	1064	13 11 26.524	−1 19 55.49	25.58 ± 0.05	5.3	$4.8^{+1.1}_{-0.9}$	(1.83)	$0.23^{+2.43}_{-0.14}$	1.2
d	HL	1760	1282	13 11 26.496	−1 20 22.08	25.06 ± 0.03	7.0	$6.0^{+1.5}_{-1.2}$	(1.83)	$2.35^{+0.33}_{-2.08}$	4.5
32a	L	2821	2671	13 11 32.191	−1 20 03.53	24.08 ± 0.01	2.0	$2.0^{+0.3}_{-0.3}$	(3.0)	0.15 ± 0.11	2.0
b	L	2637	3097	13 11 33.216	−1 20 20.90	25.56 ± 0.04	3.9	$4.3^{+1.7}_{-1.2}$	3.0^4	$3.71^{+0.46}_{-0.47}$	1.9
c	L	1416	2468	13 11 29.589	−1 21 02.83	26.15 ± 0.07	1.4	$1.2^{+0.2}_{-0.2}$	(3.0)	$3.37^{+0.43}_{-3.15}$	0.5
d	L	1796	2361	13 11 29.804	−1 20 43.35	25.13 ± 0.05	3.0	$2.2^{+0.8}_{-0.6}$	(3.0)	$0.48^{+3.61}_{-0.24}$	5.9
33a	L	1310	2140	13 11 28.449	−1 21 00.66	27.55 ± 0.11	1.3	$3.7^{+6.0}_{-2.3}$	4.58^4	$0.61^{+3.65}_{-0.45}$	2.6
b	25.2	2745	2621	13 11 31.932	−1 20 05.91	26.40 ± 0.05	4.3	$4.2^{+6.1}_{-2.5}$	(4.58)	3.79 ± 0.47	0.4
35a	L	1348	2159	13 11 28.560	−1 20 59.35	24.63 ± 0.03	1.0	$3.4^{+7.3}_{-2.3}$	1.9^4	2.95 ± 0.39	1.9
b	L	2521	3397	13 11 33.958	−1 20 32.52	24.84 ± 0.03	4.8	$6.5^{+3.3}_{-2.2}$	(1.9)	$0.03^{+3.01}_{-0.03}$	9.3
c	L	1906	2186	13 11 29.431	−1 20 34.66	25.68 ± 0.10	1.2	$0.9^{+0.2}_{-0.2}$	(1.9)	$1.52^{+0.98}_{-1.04}$	20.7

Table 5
(Continued)

ID	ID[a]	x[b]	y[b]	R.A.	Decl.	i'_{775}	Magnification[c]		Spec./Photometric Redshift[d]		
	B05	(pixel)	(pixel)	(J2000.0)	(J2000.0)	(AB mag)	Final	Range	z_{spec}[e]	z_b[f]	χ^2_{mod}[g]
36a	L	3060	2352	13 11 31.566	-1 19 45.94	25.64 ± 0.05	20.4	$20.1^{+1.3}_{-1.2}$	3.0^4	$1.04^{+0.98}_{-0.96}$	0.8
b	L	3049	2397	13 11 31.686	-1 19 47.39	26.00 ± 0.06	7.0	$6.7^{+0.5}_{-0.5}$	(3.0)	$1.84^{+0.80}_{-0.74}$	0.5
40a	L	2421	2219	13 11 30.260	-1 20 12.04	27.03 ± 0.12	1.8	$0.7^{+0.4}_{-0.3}$	2.52^4	$1.78^{+1.18}_{-1.58}$	0.7
b	L	973	1545	13 11 26.176	-1 21 03.29	25.88 ± 0.05	2.5	$2.5^{+0.1}_{-0.1}$	(2.52)	2.88 ± 0.38	1.3
41a	$\cdots$	1453	1882	13 11 27.872	-1 20 48.71	23.06 ± 0.01	2.9	$3.4^{+0.7}_{-0.6}$	$\cdots$	$0.55^{+0.15}_{-0.47}$	1.6
b	$\cdots$	2777	3795	13 11 35.522	-1 20 29.38	25.14 ± 0.03	1.8	$1.9^{+0.1}_{-0.1}$	$\cdots$	3.12 ± 0.40	0.7
c	$\cdots$	1856	2054	13 11 28.962	-1 20 34.12	99.00 ± 28.72	2.0	$2.3^{+0.2}_{-0.2}$	$\cdots$	$1.33^{+3.83}_{-0.95}$	1.5
42a	$\cdots$	2745	1541	13 11 28.672	-1 19 42.98	22.97 ± 0.01	25.7	$35.4^{+9.2}_{-7.3}$	$\cdots$	$0.53^{+2.19}_{-0.23}$	0.4
b	$\cdots$	2885	2336	13 11 31.270	-1 19 53.52	24.77 ± 0.02	103.3	$69.1^{+23.6}_{-17.6}$	$\cdots$	2.68 ± 0.36	1.3
c	$\cdots$	2403	3304	13 11 33.510	-1 20 35.89	25.66 ± 0.03	4.9	$5.0^{+0.2}_{-0.2}$	$\cdots$	2.81 ± 0.39	2.8
d	$\cdots$	1261	2357	13 11 29.035	-1 21 07.49	25.56 ± 0.03	2.2	$2.2^{+0.2}_{-0.2}$	$\cdots$	$2.52^{+0.35}_{-1.86}$	0.6
44a	$\cdots$	2030	1825	13 11 28.517	-1 20 21.38	24.49 ± 0.03	7.9	$6.2^{+1.0}_{-0.9}$	$\cdots$	$2.58^{+0.36}_{-0.55}$	1.4
b	$\cdots$	2060	3803	13 11 34.531	-1 21 02.01	25.31 ± 0.04	4.0	$5.3^{+1.4}_{-1.1}$	$\cdots$	$2.27^{+0.68}_{-2.11}$	0.5
45a	25.1	2522	3069	13 11 32.969	-1 20 25.51	25.14 ± 0.06	35.5	$\cdots$	$\cdots$	3.70 ± 0.46	1.2
b	$\cdots$	2769	3852	13 11 35.682	-1 20 30.95	26.07 ± 0.04	1.3	$\cdots$	$\cdots$	0.62 ± 0.16	5.3
46a	$\cdots$	1964	2900	13 11 31.669	-1 20 47.19	25.12 ± 0.04	22.0	$\cdots$	$\cdots$	$0.76^{+2.37}_{-0.59}$	135.4
b	$\cdots$	1711	796	13 11 24.959	-1 20 13.98	25.67 ± 0.05	3.9	$\cdots$	$\cdots$	$0.20^{+2.50}_{-0.12}$	1.5
48a	$\cdots$	2144	2779	13 11 31.558	-1 20 36.47	25.22 ± 0.05	6.4	$\cdots$	$\cdots$	$1.41^{+1.19}_{-1.27}$	0.2
b	$\cdots$	1660	868	13 11 25.104	-1 20 17.82	27.08 ± 0.11	13.0	$\cdots$	$\cdots$	$2.47^{+0.66}_{-2.10}$	1.2
49a	$\cdots$	2216	1849	13 11 28.853	-1 20 13.47	25.60 ± 0.05	2.3	$\cdots$	$\cdots$	$0.20^{+2.73}_{-0.12}$	0.7
b	$\cdots$	1852	3582	13 11 33.569	-1 21 06.73	26.28 ± 0.06	3.1	$\cdots$	$\cdots$	$2.60^{+0.40}_{-2.32}$	0.9
50a	$\cdots$	2145	3117	13 11 32.580	-1 20 43.60	26.69 ± 0.06	8.1	$6.0^{+1.7}_{-1.3}$	$\cdots$	$4.08^{+0.50}_{-0.52}$	0.4
b	$\cdots$	1485	2910	13 11 31.021	-1 21 09.08	26.59 ± 0.05	14.0	$15.9^{+1.6}_{-1.5}$	$\cdots$	$3.25^{+0.99}_{-0.42}$	0.3
c	$\cdots$	2570	2613	13 11 31.660	-1 20 13.66	28.01 ± 0.18	24.5	$39.9^{+22.9}_{-14.5}$	$\cdots$	$2.23^{+1.74}_{-2.02}$	1.7

Notes.

[a] Quotation marks indicate agreement with the B05 numbering system (where our 1a is their 1.1, etc.). "L" indicates a system added by L06, and "$\cdots$" a system added in this paper. "HL" indicates systems that were added by H06 but for which we use L06's numbering.

[b] Pixel coordinates ($0''05$ pixel^{-1}) in the original APSIS-reduced ACS images (see Section 3.5).

[c] Magnification in final model and range across ensemble. Calculated as ratios of lensed and delensed image segment areas. Ranges are only given if the image is included in at least five models.

[d] Also see Table 7 for galaxy input (spectroscopic/photometric) and output (lens model) redshifts.

[e] Spectroscopic redshift, if available. Values in parentheses are assumed from other multiple image(s). Superscripts give references: (1) Frye et al. 2002; (2) B05; (3) Frye et al. 2007; (4) L07.

[f] Bayesian photometric redshift and 95% confidence interval. Based on fits to photometry across 12 filters without subtraction of cluster galaxies.

[g] Poorness of BPZ fit: observed versus model fluxes with uncertainties.

3. MULTIPLE IMAGES

Building on previous work, we present a catalog of 135 images of 42 background galaxies. We contribute 20 new candidate multiple images of eight galaxies, along with a few tweaks to previous identifications. We discard three central demagnified images in use since B05, finding these identifications suspect; our technique is more sensitive to the positions of central images than other techniques (see Section 3.2). We add one new central image identification.

We also identify multiple knots in 42 of the galaxy images which we use as additional constraints. Constraining the positions of three non-collinear knots in an image is equivalent to constraining the precisely measured shear and magnification of that image. Our mass map solutions perfectly reproduce the observed positions of 168 multiple images of 55 knots residing within 135 images of 42 galaxies. The final set of multiple images used in this work is given in Table 5 and shown in Figure 3. Close-ups of all the images are shown in Figure 16. Additional knots are visible in these images and listed in Table 6. In this section, we discuss the multiple image identification as well as the redshifts for these systems.

3.1. Multiple Image Identification

The original analysis of the ACS A1689 images (B05) yielded 106 multiple images of 30 background galaxies. This was a truly pioneering effort as the first multiple image identifications were the most difficult. The relatively steep mass profile of A1689 near the Einstein radius produces relatively thin arcs. Thus, there are no truly obvious systems with thick multiple images as in, say, CL0024 (Tyson et al. 1998; Zitrin et al. 2009b). Only after careful study of the color image did B05 discover the image system 1–2, a pair of pale green and blue specks that repeats five times about the image, leaving no doubt as to its identification. Once these first multiple images are identified, an initial mass model may be obtained, greatly facilitating the identification of further image systems.

B05 identified many image systems, but they did not attempt to identify all. Additional systems have since been proposed, and we propose still more in this paper. Of the 30 image systems
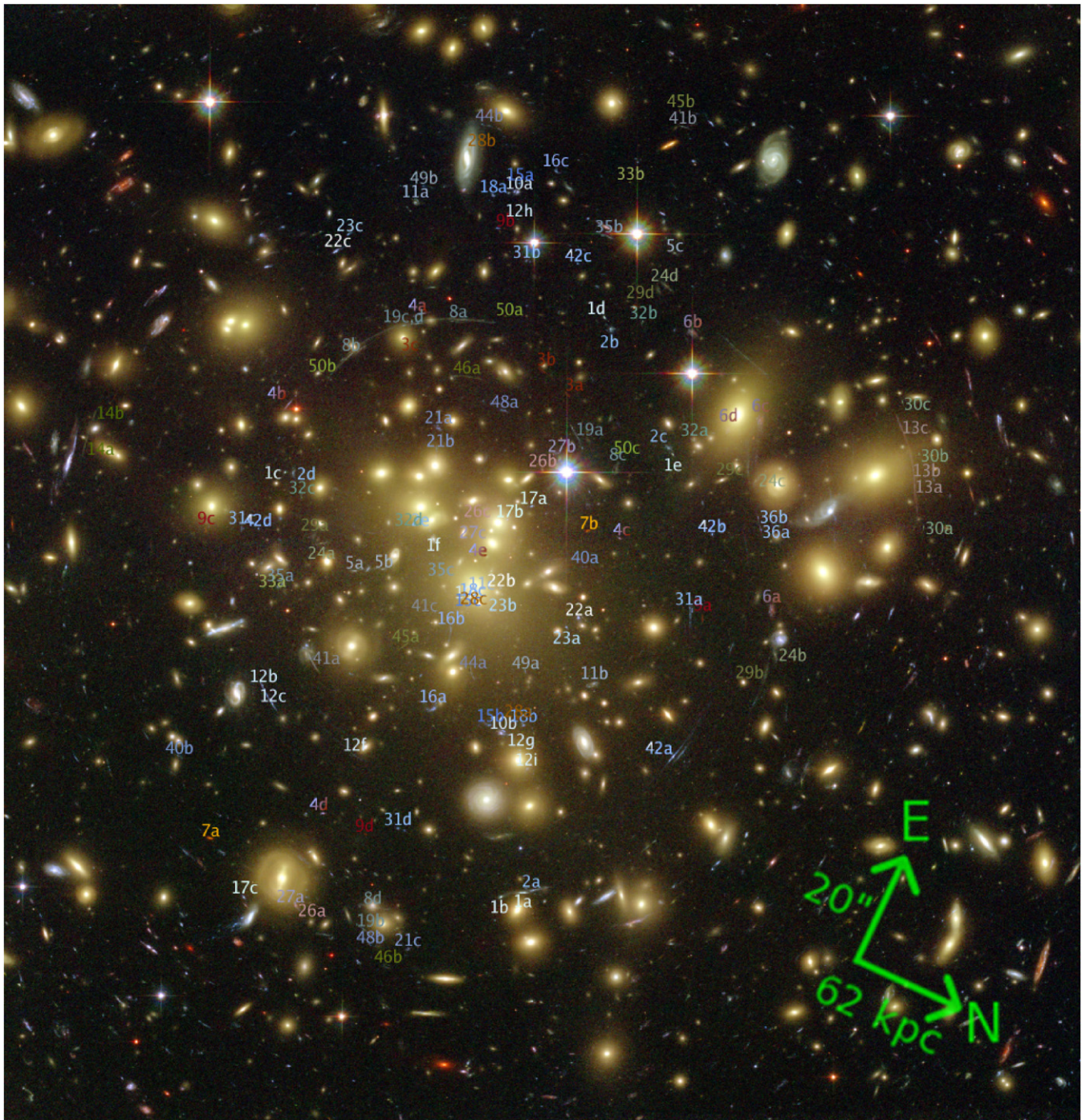
Figure 3. Multiple images in A1689 labeled on the STScI 3′.2 × 3′.3 ACS $g'r'z'$ color image. Most of the labels are directly above the images, but some have been offset slightly to minimize clutter. The exact coordinates of each image are given in Table 5. A compass provides the orientation (a 115° roll angle), while the lengths of the arrows provide the scale (20″ ≈ 62 kpc).

(A color version of this figure is available in the online journal.)

proposed by B05, doubts have been since been raised about three. We further call into question three of their central image identifications.

Z06 (their Section 8.4) experimented with excluding some image systems from their modeling on the grounds that they yielded larger than average scatter in the delensed positions. But they stopped short of calling any of B05's systems into question, as large scatter may also result from shortcomings of the mass model. Among the problem systems they cited were systems 1–2 and 15 which have ironclad identifications as multiple images

from visual inspection. Images near critical curves such as these often prove difficult to fit for conventional modeling methods, as the predicted image positions are unstable with respect to small variations in the mass model. For this reason, L07 also found it necessary to remove the giant arc (system 8) from their modeling.

Some more systematic changes to the B05 catalog were made by H06 and L07. They discarded and altered a few systems which appear to have been misidentified in the original B05 analysis. H06 (see discussion in their Section 3.3) split B05's

Table 6
Extra Knots Identified in the Multiple Images

ID[a]			x[b] (pixel)	y[b] (pixel)	R.A. (J2000.0)	Decl. (J2000.0)
4	a	1	1818	3116	13 11 32.114	−1 20 58.38
	b	1	1395	2832	13 11 30.658	−1 21 11.50
	c	1	2545	2328	13 11 30.765	−1 20 08.74
	d	1	1485	1336	13 11 26.269	−1 20 35.67
6	a	1	3093	2082	13 11 30.798	−1 19 38.71
	a	2	3092	2075	13 11 30.775	−1 19 38.61
	b	1	2803	3067	13 11 33.361	−1 20 12.75
	b	2	2801	3058	13 11 33.331	−1 20 12.65
8	a	1	1956	3098	13 11 32.255	−1 20 51.75
	a	2	1996	3108	13 11 32.342	−1 20 50.15
	b	1	1628	3000	13 11 31.495	−1 21 04.52
	b	2	1560	2961	13 11 31.281	−1 21 06.77
10	a	1	2179	3564	13 11 33.978	−1 20 51.55
	b	1	2134	1634	13 11 28.088	−1 20 12.62
16	a	1	1897	1732	13 11 28.048	−1 20 25.43
	a	2	1864	1712	13 11 27.941	−1 20 26.50
	b	1	1943	1958	13 11 28.795	−1 20 28.14
	b	2	1946	2005	13 11 28.942	−1 20 29.00
	c	1	2327	3643	13 11 34.426	−1 20 46.53
18	a	1	2095	3555	13 11 33.832	−1 20 55.16
	b	1	2206	1663	13 11 28.277	−1 20 09.97
19	a	1	2384	2716	13 11 31.708	−1 20 24.27
	a	2	2421	2644	13 11 31.543	−1 20 21.06
	b	1	1657	910	13 11 25.227	−1 20 18.84
	b	2	1613	941	13 11 25.258	−1 20 21.49
	d	1	1834	3090	13 11 32.059	−1 20 57.11
31	a	2	2807	2022	13 11 30.212	−1 19 50.39
	a	3	2814	2070	13 11 30.366	−1 19 51.09
	b	3	2233	3311	13 11 33.290	−1 20 43.73
	c	2	1199	2349	13 11 28.923	−1 21 10.12
	c	3	1207	2358	13 11 28.961	−1 21 09.95
	d	2	1762	1288	13 11 26.517	−1 20 22.11
	d	3	1785	1276	13 11 26.513	−1 20 20.82

Notes.

[a] ID numbers as in Table 5, with the third column giving the "knot number."
[b] Pixel coordinates (0″.05 pixel^{-1}) in the original APSIS-reduced ACS images (see Section 3.5).

system 12 in two: a new streamlined system 12 comprised of just 12b and 12c and a new four-image system 13 comprised of 12a, 12d, and two new counter images. (Note this offsets their numbering relative to B05 for B05's systems 13–19.) Splitting 12a and 12b into different systems was a bold proposition, given that they were known to have the same spectroscopic redshift of $z = 1.83$. But L07 concurred with this assessment (see their Section 4.2), and so do we. We adopt L07's convention of assigning the number 31 to H06's system 13, thus preserving the B05 numbering system.

B05 may have misidentified the counterimages of the fold arc 12bc, but this arc almost certainly has other counterimages. We identified three counter images 12fgh plus an image 12i which is a counter image of 12g due to strong galaxy–galaxy lensing. (Note these designations, 12fghi, were intended to avoid confusion with B05's original identifications of images 12abe. We did not intend to suggest this is a nine-image system. There are but six images in our new system 12.)

H06 also discarded B05's three-image system 20 located in the top-left corner of the image at large radius. Not only do the images fit poorly with the mass model, but the images show slightly different morphologies. L07 concurred, adding that the spectra are also somewhat different. We did not attempt to add this system to our mass model.

L07 also took issue with B05's system 25, finding a different counterimage to 25b and naming the new system 33. We concur, finding the new system a much better fit. As for B05's 25a (a greenish radial arc), we identify a new counterimage candidate at fairly large radius, and we rename the system 45.

H06 identified one brand-new system (their 31), a small pair of blue images along the fold inside the main subclump. L07 "rediscovered" this system, naming it 36. L07 also propose the following brand-new systems with numbers of images given in parentheses: 32 (4), 35 (3), 36 (2), and 40 (2). We include all of these in our mass model.

We have proceeded to identify eight new candidate systems containing a total of 20 multiple images. We have named these (with number of images given): 41 (3), 42 (4), 44 (2), 45 (2), 46 (2), 48 (2), 49 (2), and 50 (3). As mentioned above, we recycled B05's image 25a for use in our system 45, but the other 19 multiple images are brand-new identifications.

We do not have spectroscopic redshifts for our new systems; thus our two-image systems do not currently provide strong constraints. In the course of our mass modeling, we add our new systems at the end and find that our two-image systems have little effect on the mass map.

We also mention in passing H06's "system" 32, a single large but low surface brightness arc just outside the image pair 6cd in the main subclump. They were unable to identify a counterimage for the arc and neither were we. We do not utilize this arc in our modeling.

3.2. Demagnified Central Images

The identification of central images is crucial to constraining the inner mass profile of any lens. This is generally a difficult task both because central images are strongly demagnified and because this faint light is overwhelmed by the bright galaxy or galaxies which make up the lens. We have carefully modeled and subtracted most of the cluster galaxies from each of the g', r', i', and z' ACS images (K. C. Zekser et al., in preparation). The recombined galaxy-subtracted color image reveals many colored specks in the central region of the cluster. A great number of these specks are globular clusters belonging to A1689 (Mieske et al. 2004, 2005). The rest may be demagnified multiple images. Aside from sorting out this confusion, we also have to contend with residuals which persist from the galaxy subtraction. Correct identification of a central multiple image relies on finding the proper color speck (or group of specks for paired image systems) at approximately the location predicted by the model. Often we find several specks of approximately the correct color in approximately the predicted location. Thus, it should not be surprising when we claim that a few mistakes may have been made previously. Conventional mass modeling has allowed these mistakes to go unnoticed by B05 and in subsequent studies.

As mentioned above, conventional modeling methods may be very sensitive to the positions of images in regions of high magnification. Conversely, they generally will not be very sensitive to the exact positions of demagnified images. Our model-predicted positions for the central images 7c, 8e, and

19e are "only" offset by $\sim 2\rlap{.}''5$, $7''$, and $2\rlap{.}''5$ from the B05 positions, respectively. Thus, these offsets may be easily missed by routines that minimize offsets in the image plane. (Note that attempts may be made to normalize the offsets by the local magnification, but this is often not attempted as it can lead to instability in the optimization routine.) If optimization is instead performed in the source plane (technically inferior but much quicker), the method might actually be more sensitive to the offsets of central images. L07 do find higher than average $(0\rlap{.}''4)$ offsets in the source plane for systems 7 $(1\rlap{.}''09)$ and 19 $(0\rlap{.}''48)$. And as mentioned above, L07 found such large errors for system 8 that they excluded it from their analysis. The incorrect identification of 8e, $7''$ from the position we predict, may have contributed to their errors as much as the unstable model positions of 8ab (near the critical curve for that redshift). The high offset for the three-image system 7 may have raised alarms in L07's analysis. But they find similarly large offsets for the pair of systems 26–27, and we find no quarrel with this pair. The 26–27 pair does, however, strongly require asymmetry in the center of the mass map, which had not been observed by previous authors. In conventional mass modeling, it is difficult to say when a larger than average offset is a misidentification and when it may simply indicate a shortcoming of the mass model.

LensPerfect, on the other hand, is extremely sensitive to the relative positions of all of the central images. For example, a central image incorrectly identified to the wrong side of another central image is generally disastrous for the mass model, causing the deflection field to get tangled in itself.

We reexamined all of B05's central image identifications. The pair 1f–2e is confidently identified by the images' colors and proximity to one another. As for the rest (4e, 7c, 8e, 19e, 10–15–18c, 11c, 22–23b, 26–27c, 32d, 35c),[10] we purged them all from the image list and obtained a mass model solution without them. We then re-added the multiple images one by one to our model. We found that a few central images (7c, 8e, 19e) did not fit well with the rest, producing aphysical models when added (even after all of the source positions were allowed to shuffle to new positions in search of a physical model). We are unable to securely identify replacement central images for systems 7, 8, and 19, as there are too many similarly colored specks in the area which confuse the issue.

Red demagnified central images stand out more and are easier to identify. We identify one new central image candidate 28c which we incorporate into our mass model. It fits easily into our model, not significantly affecting it.

3.3. Additional Knots

With LensPerfect we obtain mass map solutions which delens the input centroids of all images of a given system to the exact same position in the source plane. But this alignment does not guarantee that the delensed images will have the same shape or orientation. Thus, we identify additional knots where possible in the multiple images. These knots are labeled in Figure 16. If the delensed positions of these knots do not align well naturally given our mass model, then we add them as constraints and force them to align. In Table 6, we give the positions of these additional knots which we have constrained in our mass model (in addition to the centroids/primary knots listed in Table 5).

---

[10] Dashes link objects (e.g., 10, 15, and 18) assumed to be in physical groups with redshifts constrained to be equal in our model. We are *not* referring to objects 10 through 18, inclusive.

These knots are also labeled in green in Figure 17. In all, our model incorporates 168 observed (lensed) positions of 55 knots.

These additional constraints further improve the accuracy of our mass map (assuming our multiple image identifications are robust, as we believe they are). Constraining three non-collinear knots in an image effectively uses both the observed shear and relative magnification of that image. In Coe et al. (2008), we compared mass maps of MS1358 given a single multiply imaged galaxy both with and without additional knots constrained. The additional knots add significant detail to the mass map.

3.4. Redshifts

In the original B05 analysis, spectroscopic redshifts were available for five systems: 1ad 3.04, 2a 2.54, 7a 4.87, 10a 1.37, and 12ab 1.82. Since then, system 12 has been split in two by H06 (our 12 and 31) and the redshift of 10a has been called into question by L07, with the net result being that we still had five systems with available redshifts. Our initial analyses made use of these spectroscopic redshifts alone.

L07 have since contributed spectroscopic redshifts for another 19 systems (4a, 5ac, 6ab, 10–15–18a, 11a, 14a, 17c, 19d, 22a, 24c, 29d, 30c, 32b, 33a, 35a, 36a, 40a), bringing the total to 24 systems with spectroscopic redshifts (Table 5). We have compared our results before and after incorporating these redshifts into our mass modeling. We find the substructure shifts somewhat, but overall the mass models appear to be very similar qualitatively. Our "optimized" redshifts (described below) were generally close to the spectroscopic redshifts, with a scatter of $\Delta z \approx 0.06(1 + z_s)$ after pruning one outlier.

For those systems without spectroscopic redshifts, we use photometric redshifts (Section 2) as initial guesses in our optimization routine (Section 4). We allow these redshifts to wander but they incur a penalty for doing so. A rough uncertainty ($\Delta z = 0.5, 0.7, 1.0, 2.0$) is assigned to each redshift according to our relative confidence in it, and deviations from the input values are divided by these uncertainties. Given these normalized deviations, we then take the rms and add this to our penalty evaluation. As we are modeling 43 image systems, the total rms will not be very sensitive to single outliers. This approach will allow individual redshifts to wander unacceptably far. In order to "leave no redshift behind," we also find the maximum normalized deviation and add this to our penalty function. Our input redshifts and uncertainties along with final optimized redshifts for each system are given in Table 7.

We could attempt to penalize redshift deviations more scientifically by using the redshift probability distributions $P(z)$ returned from BPZ for each object. However, photo-z uncertainties are often underestimated by current methods including BPZ (Hildebrandt et al. 2008). Thus, we prefer to assign simple and rather generous uncertainties to the redshifts and allow them to naturally obtain their optimal values based on the mass model.

Some sets of images appear to be physically linked: 10–15–18, 22–23, 24–29, and 26–27. During our optimization procedure, we find that within each of these sets, all of the redshifts gravitate toward common values (10–15–18: 2.00–2.14–1.96; 26–27: 1.98; 24–29: 1.91, 22–23: 1.4, 1.46). Thus, we take the liberty of fixing all of the redshifts to be equal within each set. For example, when the redshift of object 10 is optimized, the redshifts of objects 15 and 18 are forced to follow. We believe these systems to be physically linked but any one of them might instead be a chance alignment. Object 15,

Table 7
Multiple Image Systems

ID	Number of Images	Knots per Image	Input Order	Spectroscopic Redshift	Ref.[a]	Input Redshift[b]	Output Redshift[c]
1	6	1	1	3.04	2, 3	3.04	3.04
2	5	1	2	2.53	3	2.54	2.54
3	3	1	23	$\cdots$	$\cdots$	5.47 ± 0.7	5.490
4	5	2	7	1.1	4	1.1	1.1
5	3	1	13	2.6	4	2.6	2.6
6	4	3	12	1.1	4	1.1	1.1
7	2	1	5	4.87	1	4.87	4.87
8	4	3	10	$\cdots$	$\cdots$	1.8 ± 0.5	2.224
9	4	1	4	$\cdots$	$\cdots$	5.16 ± 0.5	4.707
10	3	2	18	1.83	4	1.8	1.8
11	3	1	25	2.5	4	2.5	2.5
12	6	1	30	1.83	2, 4	1.83	1.83
13	3	1	31	$\cdots$	$\cdots$	1.02 ± 0.5	1.532
14	2	1	32	3.4	4	3.4	3.4
15	3	1	19	1.8	4	(10)	1.8
16	3	3	14	$\cdots$	$\cdots$	2.01 ± 0.5	1.635
17	3	1	26	2.6	4	2.6	2.6
18	3	2	20	1.8	4	(10)	1.8
19	4	3	11	2.6	4	2.6	2.6
21	3	1	15	$\cdots$	$\cdots$	1.78 ± 0.5	1.065
22	3	1	16	1.7	4	1.7	1.7
23	3	1	17	$\cdots$	$\cdots$	(22)	1.7
24	4	1	8	2.6	4	2.6	2.6
26	3	1	21	$\cdots$	$\cdots$	(27)	2.388
27	3	1	22	$\cdots$	$\cdots$	1.74 ± 0.5	2.388
28	3	1	24	$\cdots$	$\cdots$	5.45 ± 0.7	4.451
29	4	1	9	2.5	4	2.5	2.5
30	3	1	33	3.0	4	3.0	3.0
31	4	3	3	1.83	2, 4	1.8	1.8
32	4	1	6	3.0	4	3.0	3.0
33	2	1	27	4.58	4	4.5	4.5
35	3	1	28	1.9	4	1.9	1.9
36	2	1	34	3.0	4	3.0	3.0
40	2	1	29	2.52	4	2.5	2.5
41	3	1	37	$\cdots$	$\cdots$	2.5 ± 2.0	5.357
42	4	1	35	$\cdots$	$\cdots$	2.0 ± 2.0	2.222
44	2	1	38	$\cdots$	$\cdots$	2.0 ± 2.0	3.210
45	2	1	39	$\cdots$	$\cdots$	2.5 ± 2.0	5.359
46	2	1	40	$\cdots$	$\cdots$	2.5 ± 2.0	1.714
48	2	1	41	$\cdots$	$\cdots$	2.0 ± 2.0	1.456
49	2	1	42	$\cdots$	$\cdots$	2.0 ± 2.0	1.645
50	3	1	36	$\cdots$	$\cdots$	2.5 ± 2.0	3.029

Notes. Our mass model was built by iteratively adding our multiple image systems in the order given here. Any additional knots were added immediately after inclusion of the "main knot" for that system.
[a] Reference for $z_{\rm spec}$: (1) Frye et al. 2002; (2) B05; (3) Frye et al. 2007; (4) L07.
[b] Input redshifts with rough uncertainties where allowed. (Spectroscopic redshifts are given zero uncertainty.) Redshifts of some systems are tied to other systems with numbers given in parentheses. (For example, the redshift of system 26 is tied to that of system 27 in the optimization.)
[c] Final model redshift, optimized if input value included uncertainty.

for example, did obtain a slightly higher redshift than 10 and 18 when left free as noted above.

Objects 1–2 also appear to be physically linked, but our models say otherwise. The objects do have different spectroscopic redshifts, but that obtained for object 2 is somewhat uncertain, as its spectra appear to show absorption from three separate systems along the line of sight at redshifts 2.53, 2.87, and 3.04 (Frye et al. 2007). We tried fixing the redshift of object 1–3.04 and giving object 2 an initial guess of the same redshift ($z = 3.04$) but allowing it to wander (incurring a small penalty for doing

so). A lower redshift of $\sim$2.5 was clearly preferred for system 2, thus supporting the spectroscopic redshift of 2.53 preferred by Frye et al. (2007).

3.5. Coordinate System

The final catalog of multiple images used in our modeling is given in Table 5. We provide coordinates in both (R.A., decl.) and in (x, y). Our (x, y) coordinate system is based on the original APSIS (Blakeslee et al. 2003) ACS GTO pipeline reductions. These images are 4421×4525 pixels (1 pixel = $0\rlap{.}''05$). Our bottom-left pixel is centered at (1,1) as in SExtractor and ds9. North and east are 115° clockwise from up and left, respectively.

Based on the central 3853×4000 area of these images, STScI released a $g'r'z'$ color image.[11] An offset of (350, 232) may be subtracted from our coordinates to obtain coordinates in the color image. The ACS images were later reprocessed by APSIS yielding images 4379×4481 pixels. The improvements included better correction for the geometrical distortion of the images. Nevertheless, the offset in coordinates between the original and subsequent processed images is a nearly constant (21, 22) across the entire image, only deviating by a pixel in x in the top-left and bottom-right corners.

4. LensPerfect MASS MAP RECONSTRUCTION

LensPerfect is a novel approach to gravitational lens mass map reconstruction. The 100+ SL features produced by A1689 present us with a large puzzle. We must produce a mass model of A1689 with the correct amounts of mass in all the right places to deflect light from 30+ background galaxies into multiple paths such that they arrive at the 100+ positions observed.

Most SL analysis methods construct many possible models and then iterate to find that which best matches the data. LensPerfect instead uses direct matrix inversion to find perfect solutions to the input data. Using LensPerfect, we may, for the first time, obtain a mass map solution which perfectly[12] reproduces the input positions of all 100+ multiple images observed in A1689.

LensPerfect makes no assumptions about light tracing mass. Non-LTM models are common in analyses of WL or combined SL + WL (e.g., Bradač et al. 2006; Diego et al. 2007; Merten et al. 2009; Deb et al. 2009). Dedicated SL analysis methods are able to process greater numbers of multiple images. Non-LTM SL analysis methods include PixeLens (Saha & Williams 2004; Coles 2008), SLAP (Diego et al. 2005a, 2005b), and methods developed by Liesenborgs et al. (2006, 2009) and Jullo & Kneib (2009). (The latter includes both LTM and non-LTM components.) We note that non-LTM methods are also used in SL modeling of extended images lensed by individual galaxies (e.g., Vegetti et al. 2009). Non-LTM multipole expansion models have also been applied to galaxy (Evans & Witt 2003; Congdon & Keeton 2005) and group lenses (Alard 2009).

LensPerfect was made possible by a recent advance in the field of mathematics (Fuselier 2006, 2007). The method was described in detail in Coe et al. (2008). Here, we provide a brief outline of the procedure.

Image deflection by a gravitational lens is governed by a few simple equations (e.g., Wambsganss 1998). Given the bend

---

[11] http://hubblesite.org/newscenter/archive/releases/2003/01/
[12] Again, while the image positions do have (small) observational uncertainties of a pixel ($0\rlap{.}''05$) or so, our solutions do perfectly fit the data as input. We may vary the image positions within this uncertainty to produce other valid solutions, however this is not a significant uncertainty in our models.

angle $\vec{\alpha}$ of light due to mass predicted by Einstein (1916), we can derive the deflection of light due to a mass sheet with surface density κ as a function of position $\vec{\theta}$ in the lens/image plane:

$$\vec{\alpha}(\vec{\theta}) = \frac{1}{\pi} \int d^2\vec{\theta}' \kappa(\vec{\theta}') \frac{\vec{\theta} - \vec{\theta}'}{|\vec{\theta} - \vec{\theta}'|^2}, \qquad (1)$$

with the simple corresponding inverse relation:

$$\nabla \cdot \vec{\alpha} = 2\kappa. \qquad (2)$$

The surface density $\kappa = \Sigma/\Sigma_{\mathrm{crit}}$ is defined in units of the critical density at the epoch of the lens. The critical density is that generally required for multiple images to be produced. It is a function of source redshift as given by

$$\Sigma_{\mathrm{crit}} = \frac{c}{4\pi G} \frac{D_S}{D_L D_{\mathrm{LS}}}, \qquad (3)$$

involving a ratio of the angular-diameter distances from observer to source $D_S = D_A(0, z_S)$, observer to lens $D_L = D_A(0, z_L)$, and lens to source $D_{\mathrm{LS}} = D_A(z_L, z_S)$. For a flat universe ($\Omega = \Omega_m + \Omega_\Lambda = 1$), angular-diameter distances are calculated as follows (Fukugita et al. 1992, filled beam approximation; see also Hogg 1999):

$$D_A(z_1, z_2) = \frac{c}{1 + z_2} \int_{z_1}^{z_2} \frac{dz'}{H(z')}, \qquad (4)$$

where the Hubble parameter varies with redshift as

$$H(z) = H_0 \sqrt{\Omega_m (1 + z)^3 + \Omega_\Lambda}. \qquad (5)$$

(Formulae for non-flat cosmologies can be found in Coe & Moustakas 2009, for example.)

From simple geometry, we find that the deflection angle $\vec{\alpha}$ (and thus the critical density Σ_{crit}) is a function of redshift. The deflection is greatest ($\vec{\alpha}_\infty$) for a source at infinite redshift. For sources at less than infinite redshift, this deflection is reduced by the distance ratio:

$$\vec{\alpha} = \left(\frac{D_{\mathrm{LS}}}{D_S} \right) \vec{\alpha}_\infty. \qquad (6)$$

Thus, the problem of mass map reconstruction can be reduced to determining the deflection field with all deflections scaled to a common redshift (e.g., $\vec{\alpha}_\infty$), at which point we simply take the divergence and divide by 2 to obtain the mass map (Equation (2)). The deflection field $\vec{\alpha}(\vec{\theta}) = \vec{\theta} - \vec{\beta}$ may be measured at the multiple image positions $\vec{\theta}$ once source positions $\vec{\beta}$ are determined. However, in order to take its divergence, the deflection field must be solved for as a continuous function of position (or at least defined on a regular grid). Our interpolated deflection field must also be curl-free (see, e.g., Coe et al. 2008).

Only recently were the mathematical tools developed that enable us to obtain a curl-free interpolation of a vector field (Fuselier 2006, 2007). The technique uses direct matrix inversion to obtain a solution which exactly matches the vectors at the given data points and interpolates or extrapolates it elsewhere. The solution is composed of radial basis function (RBFs) each placed at the position of an observed multiple image. Each basis function has two free parameters (amplitude and rotation) *equal*

to the number of constraints (the x and y coordinates of the image). While some non-LTM methods have many more free parameters than constraints, ours does not.

In gravitational lensing, our vector (deflection) field is not defined until we assume source positions $\vec{\beta}$ for our lensed galaxies. As we add each galaxy to our model, we can obtain a good initial guess for each $\vec{\beta}$. We then perturb all of our source positions. Each arrangement of source positions yields a new mass map. Iterating over various arrangements of source positions, we find a range of mass maps all of which perfectly reproduce the observed image positions. Among these, we select the "most physical" mass map using a set of non-restrictive criteria. Aside from the requirement that the mass map be positive, these criteria (described in detail in Coe et al. 2008) promote mass maps which are smooth, decrease outward from the center on average, and are azimuthally symmetric (small scatter in radial bins, with extra penalties for "tunnels").

Our optimization routine does not check for and penalize spurious additional images due to every proposed model. This is generally very computationally expensive, although such penalties have been implemented elsewhere (Liesenborgs et al. 2007). However, we do verify that our final solutions produce no spurious additional images.

Lensing generally constrains the projected mass within the Einstein radius, or more precisely, the region within the multiple image positions. This region is known as the "convex hull" in the language of our interpolation scheme. Outside the convex hull, our solutions are ill defined and in fact drop off to zero (and even negative values) too quickly. Our mass models should generally be disregarded outside this region.

Since publishing the LensPerfect method paper (Coe et al. 2008), we have made small changes in the exact implementation of these penalties and their relative weights. And where (for the purposes of calculating penalties only) we had evaluated the mass map on a 41×41 grid we now evaluate it on a finer 81×81 grid within the convex hull and a coarser 21×21 grid outside. (With the 41×41 grid, we found one particular "tunnel" was escaping detection.) Finally, we have added the redshift penalty function as described already in Section 3.4.

We emphasize that our mass models are not "grid based." The RBFs are instead placed at the positions of the multiple images, as described above. The resulting mass model has a smooth functional form and can be calculated at any desired coordinates. However, in order to evaluate and present the results, we generally calculate the mass model on a regular grid.

5. MASS MODELS

Here, we present non-LTM mass models which perfectly reproduce the observed positions of 168 multiple images of 55 knots within 135 images of 42 galaxies, strongly lensed by A1689. We stress that there is no unique solution, and we do obtain a range of solutions which allow us to estimate our uncertainties (Section 5.2). However, first we present the most "physical" solution found by our optimization scheme described above. This optimization took 2 weeks to run on a MacBook Pro laptop. The process runs quickly at first (a few minutes per galaxy added) but slows as more galaxies are added. Galaxies were added in the order presented in Table 7.
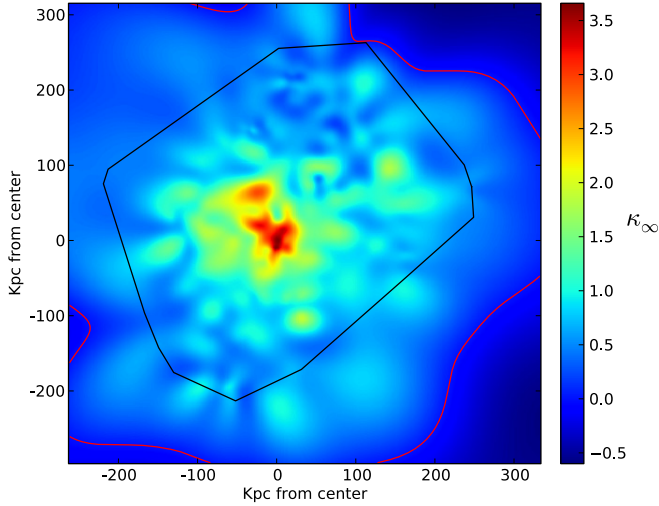
Figure 4. Mass map solution for A1689 which perfectly reproduces the 168 observed (strongly lensed) positions of 55 galaxy knots/centroids. Mass is plotted in units of κ_∞ (critical density for a source at $z_s = \infty$) and cut to the same $3.'2 \times 3.'3$ field of view as the STScI color image (previous and following figures). The black line indicates the convex hull. Multiple images are found within this region. Outside this region, our solution is highly uncertain and in fact falls off to zero too quickly. A red line marks the $\kappa = 0$ contour. We stress that this solution is not unique, but had the highest "physicality" of all solutions we explored. Angular-diameter distances are given along the axes.

(A color version of this figure is available in the online journal.)

5.1. Most Physical Mass Model

In Figure 4, we present our most physical SL mass model of A1689. The mass map contours are laid over the ACS STScI $g'r'z'$ color image in Figure 5. Our model is constrained best near the multiple images (shown in pink), interpolated between them, and is highly uncertain where it is extrapolated outside the outermost multiple images (our "convex hull"), traced in white in Figure 4 and black in Figure 5. In fact, our model falls off to zero too quickly outside the convex hull.

From inspection of Figure 5, we find that our mass model resolves halos of perhaps 10 or so galaxies which are members of A1689. Although we have made no assumptions about LTM, much of our mass model's substructure does coincide with luminous galaxies. Determining masses for these individual galaxy halos would be useful though far from trivial, as we discuss in Section 7.

There are, however, some potentially interesting offsets between mass clumps and luminous galaxies. For example, the mass near the BCG appears more pinched than the distribution of galaxies just above and to the left. Several multiple images (plotted as pink squares) are present in this region lending confidence to our mass model there. Furthermore, when we tested our method on simulated lensing with a similar mass distribution (Coe et al. 2008), our recovered mass maps exhibited no such pinching.

More quantitative and robust conclusions about the alignment of mass and light will await future work (Section 7). We will perform tests to determine how robustly substructure clumps are identified and their positions determined.

We estimate that our mass map resolves substructures ~23 kpc across within $R_E \sim 150$ kpc of the core (angular-diameter distances). This estimate is based on the density of multiple images, $Nd^2 = \pi R_E^2$, where $N = 135$ images, and we find the average separation among these to be $d \approx 23$ kpc. Each

multiple image provides a constraint on our deflection field and thus our mass model. The observed multiple images are more densely packed in some regions; thus the mass map resolution will be greater there and lesser elsewhere.

We have yet to verify the resolution yielded by our analysis, but if confirmed, this would be the highest resolution mass map to date of any galaxy cluster without assuming LTM. Leonard et al. (2007) present an SL + WL mass map of A1689 with pixels ~65 kpc across. Saha et al. (2006) and Jullo & Kneib (2009) use smaller pixels but computational issues limit them to ~30 multiple images per solution. We estimate their effective resolution to be ~50 kpc, or about one-fourth our two-dimensional resolution (half along each axis). By using four times the number of constraints (multiple images), we obtain a mass model with four times the resolution.

Finally in Figure 17, we show our multiple images as delensed to the source plane by our mass model. Note that each constrained knot in each system is delensed to the same source position in each multiple image. To be clear, we do properly model extended images as the multiple knots in *each* image map back to different locations in the source plane. For example, in the large arc (8ab), three distinct knots are identified and constrained in each image (a and b). Knots 8a0 and 8b0 map back to one point in the source plane, 8a1 and 8b1 map back to another, and 8a2 and 8b2 map back to a third point in the source plane.

5.2. Mass Model Ensemble and Uncertainties

The mass model solution presented above is not unique. Using the optimization procedure described in Section 4, we explored a wide range of source positions and redshifts, and found a set which produced this most "physical" mass map according to our criteria and without letting the redshifts stray too far from their input values.

We estimate the uncertainties in our mass model by exploring an ensemble of mass model solutions. In future work, we will develop algorithms to explore this solution space more thoroughly, as we describe in Section 7.

Here, we settle for a proxy ensemble of mass models, based on a broad but non-exhaustive search of our parameter space. This ensemble consists of 54 solutions which we obtain as we add galaxies building up to our final "best" solution. The first model in our ensemble is optimized given systems 1 and 2 only, and our last includes all 55 knots.

It is unclear whether this technique should be expected to overestimate or underestimate somewhat our actual uncertainties. We include too broad a range of solutions by including those that only fit some of the data, yet we may not be thoroughly exploring the solution space.

This technique does capture some of the systematic uncertainties which would result from adopting various subsets of the multiple image systems. Previous authors have done just that: used subsets of our multiple images. In previous work, there has also been some variation in these identifications. One or more of the systems presented in our work may yet prove incorrect, and we capture some of those uncertainties here.

Our estimated uncertainties on the radial mass profile appear to have the correct form. Mass enclosed within the Einstein radius $R_E \sim 47''$ is constrained more tightly than mass within other radii (Section 6.1).

The exact structure we resolve in the center is sensitive to the identifications of demagnified central images, which can be fairly uncertain. However, we believe that our modeling method
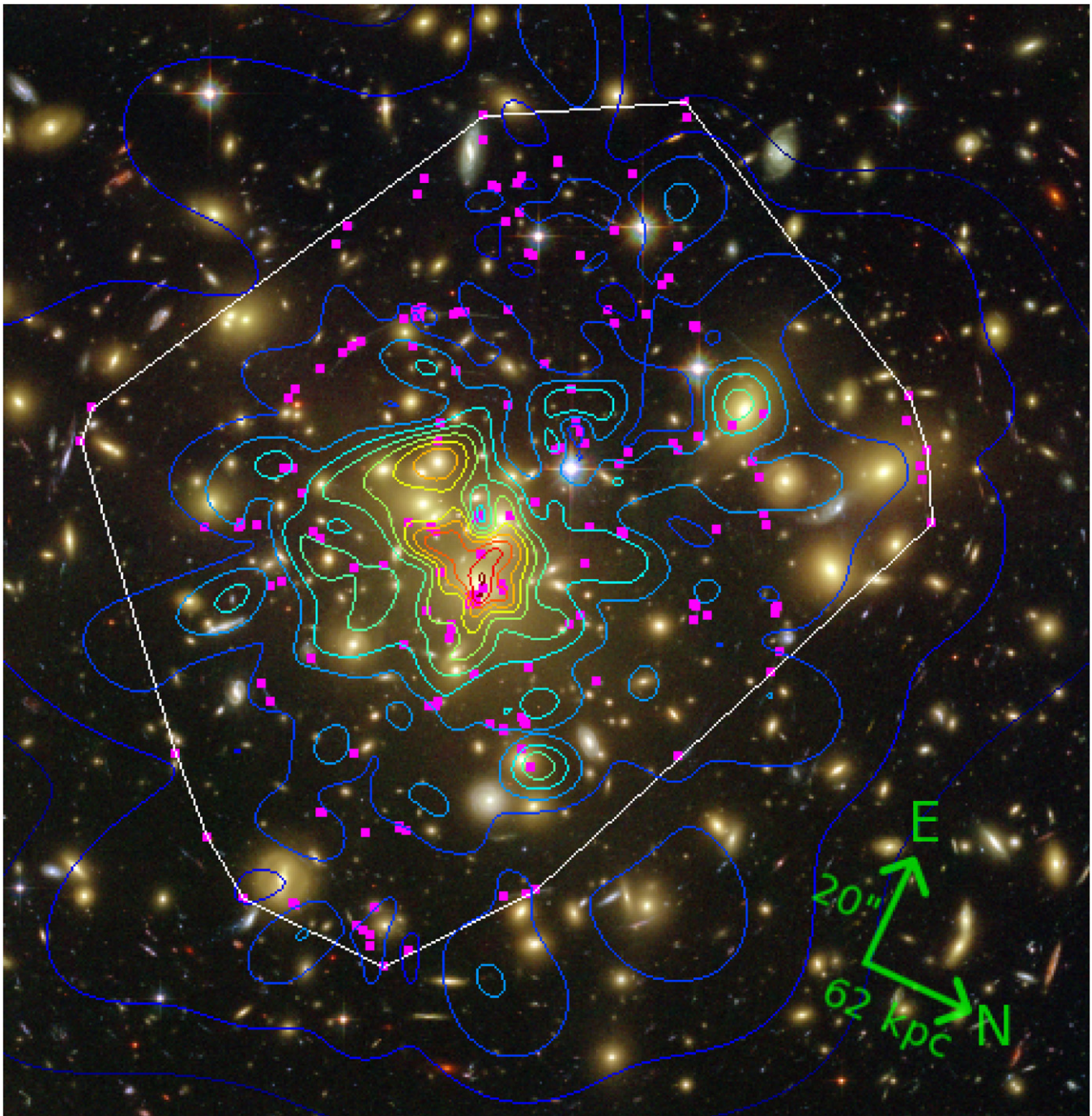
Figure 5. Mass map contours in units of $\kappa_\infty = 1/3$ laid over the $3'.2 \times 3'.3$ STScI ACS $g'r'z'$ color image. The outermost contour, $\kappa_\infty = 0$, was also plotted in the previous figure. Pink squares indicate the 135 multiple image positions all perfectly reproduced by our model, and the white line indicates the convex hull. Outside this region, our solution should be disregarded. This solution is not unique but was the "most physical" we found.

(A color version of this figure is available in the online journal.)

enables robust identification of central images. As discussed in Section 3.2, we have reexamined the B05 central image identifications, purged those which do not fit well with the rest, and identified a new central image candidate (28c) which we include in our model.

We remark that in general, non-LTM methods probably overestimate uncertainties while LTM methods probably underestimate them somewhat. LTM methods do not explore the full range of solutions (including asymmetries and other deviations from LTM) which may reproduce the data. Furthermore, they are sometimes forced to discriminate between a "best" solution which reproduces the data at, say, 50σ ($2''.5$), and "deviant" solutions which reproduce the data at, say, 60σ ($3''.0$). Non-LTM methods, on the other hand, may include, at worst, a broad range of unphysical solutions or, at least, solutions which do not take advantage of the strong observational priors available, namely, the observed positions of the lensing galaxies. An ideal method would use LTM as a prior while allowing for deviations (Section 7). This prior might be referred to as "LATM," or light *approximately* traces mass.
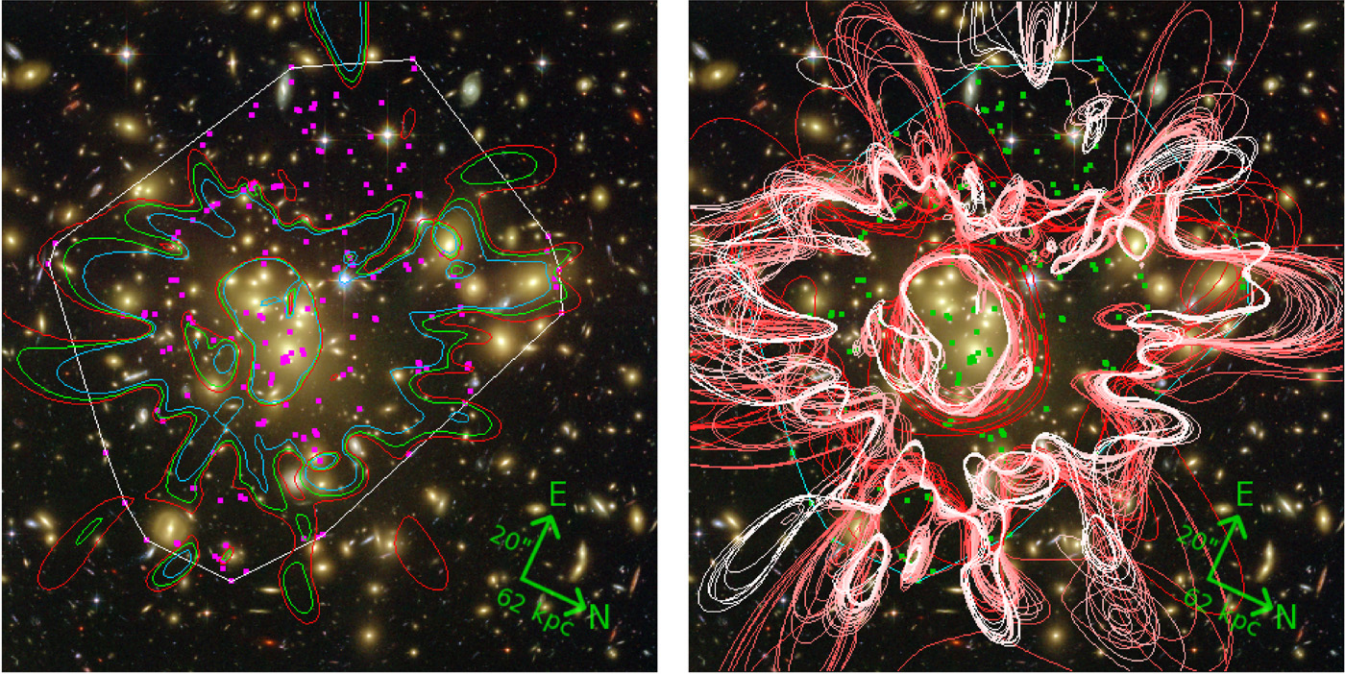
Figure 6. Left: critical curves for sources at redshifts $z_s = 1$, 2, and 7 laid over the $3\rlap{.}'2 \times 3\rlap{.}'3$ STScI ACS $g'r'z'$ color image. The loops in the curves are probably too broad, an artifact of the insufficiently resolved substructure clumps in our models. (Compare the curves with the pink squares indicating the multiple image positions which provide model constraints.) Given additional multiple images (or a well-informed prior such as LATM), finer substructure would be resolved, yielding tighter and more precise critical curves. Right: the great freedom in our models allows for broad variation in the critical curve shapes. We plot $z_s = 7$ critical curves for all solutions in our ensemble, from that which fits two multiple image systems (dark red) to our final solution (shown in white) which fits all 55 systems, including multiple knots per galaxy. The variation in magnification is such that points on our final critical curve should expect to have $\mu > 6$ 68% of the time. This would increase for a better constrained model.

(A color version of this figure is available in the online journal.)

5.3. Magnification Estimates

In Table 5, we provide a magnification estimate for each multiple image. The "final" magnifications come from our final lens model and are our best estimates. We also provide the range of magnifications (mean and standard deviation) for each object in our ensemble of models.

Each magnification is calculated as the ratio of the areas of the lensed (observed) and delensed image segments (as defined in Figures 16 and 17). We note the magnifications can vary considerably from pixel to pixel across each image such that extracting model magnifications instead at individual points would lead to large deviations from our values. Each image was delensed assuming the system redshifts in Table 7.

Based on modeling of simulated data, we expect our magnification estimates to be scattered by ∼30%–40% about the true values for reported $10 < \mu < 100$. This estimate is independent of the uncertainties quoted in Table 5. Here, we only tested a single known mass distribution similar to A1689 (as tested in Coe et al. 2008) which we modeled using 135 simulated multiple images. In this isolated test, we found only a slight bias of ∼10% low for our measured magnifications $10 < \mu < 100$. In the future, we will perform more detailed tests to better quantify our expected accuracies and precisions.

Also note that we expect our magnification estimates to be more accurate where there are many multiple images (model constraints) and less accurate where there are fewer images, especially along the outskirts (image 7a, for example).

We find the demagnified photometry of each galaxy to be very inconsistent among its multiple images. Photometric contamination from cluster galaxies is most likely to blame

(see also Alard 2010). Unfortunately, our galaxy modeling and subtraction does not solve this problem. The specific techniques used here performed well in revealing background objects but left significant photometric artifacts.

In Figure 6, we plot the critical curves for sources at redshifts $z_s = 1$, 2, and 7. The exact shapes of the critical curves are not well constrained by the data alone. They are sensitive to the exact distribution of substructure in the mass map, which for this purpose is not resolved sufficiently by our models given the number of multiple images. The critical curves would be better constrained by additional multiple images or a well-informed prior on the mass distribution (such as LATM). Even in this limiting case of broad model freedom, we find that points along our $z_s = 7$ critical curve can expect to have $\mu > 6$ 68% of the time.

6. MASS PROFILE AND CONCENTRATION

As discussed in Section 1, recent studies show that galaxy clusters formed in nature may be more centrally concentrated than their counterparts formed in simulations. In this section, we obtain new estimates for the mass–concentration of A1689. Our results support previous analyses which claim A1689's concentration is higher than expected. We derive these concentration estimates from fits of NFW profiles simultaneously to our SL mass model and WL data published elsewhere. These profiles do simultaneously fit both the SL and WL data well, however there is a slight tension between the two as described in Section 6.2. First, in Section 6.1, we examine our SL mass profile in detail.
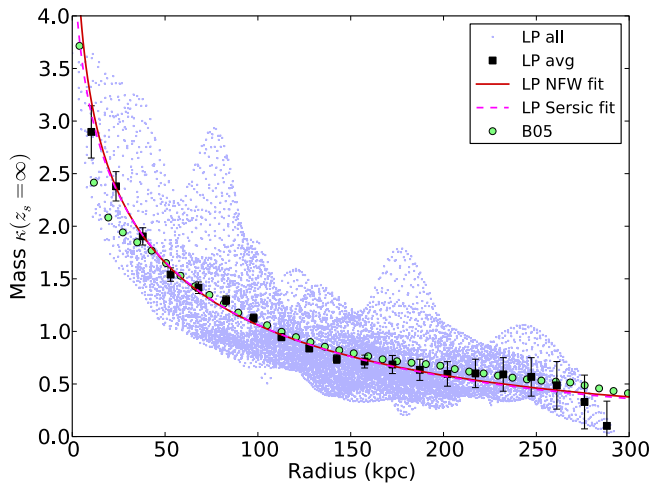
Figure 7. Our mass map fit to NFW and Sérsic profiles. For all points within our convex hull, we plot in light blue $\kappa(z_s = \infty)$, the projected surface mass density in units of critical density for a source at infinite redshift. Binned averages are plotted with uncertainties measured as the scatter among an ensemble of solutions. Our best NFW fit is plotted as the red line. The mass profile obtained by B05 is also plotted for comparison.

(A color version of this figure is available in the online journal.)

Figure 8. A1689 projected mass within a cylinder as a function of radius R. The mass profile of our best model is plotted as the dashed line while the shaded region gives the mean and rms of the ensemble. Note the mass is especially well constrained within $R \sim R_E$. The radii of the multiple images are plotted along the bottom. Those along the convex hull are plotted in red. Four central images are outside the range of the plot at small radius.

(A color version of this figure is available in the online journal.)

6.1. Profile Fits to the Strong Lensing (SL) Data

Clusters formed in simulations have mass profiles generally well described by NFW (Navarro et al. 1996) or Einasto/Sérsic (Navarro et al. 2004) profiles (e.g., Navarro et al. 2010). These profile fitting functions are described in Appendix A with further details given in Coe (2010).

In Figure 7, we plot our projected mass density radial profile $\kappa(R)$ with our origin defined as the location of our density peak which corresponds to the location of the BCG. We plot the mass profile from B05 for comparison and find good agreement even though the analysis methods are very different (including LTM versus non-LTM). For a similar recent comparison, see Zitrin et al. (2010b).

Overplotted in Figure 7 are our best NFW ($r_s = 338$ kpc, $c_{200} = 7.6$ [$c_{\rm vir} = 9.6$]) and Sérsic ($R_e = 692.8$ kpc, $\kappa_e = 0.1007$, $n = 2.148$ [$b_n = 3.968$]) fits to the SL data alone. The two fits track each other very closely, although the more flexible Sérsic profile does allow for a slightly shallower central slope. We could allow the central slope of our NFW profile to vary with a three-parameter "generalized NFW profile" (Zhao 1996; Wyithe et al. 2001), but we do not explore this here.

Rather than fitting to $\kappa(R)$ as is common, we can reduce the uncertainties of our NFW fit parameters by fitting to $M(<R)$. The former is projected mass surface density at a given radius R, while the latter is total projected mass *enclosed* within a cylinder of radius R. Fits to $M(<R)$ are fairly common as well (e.g., H06; L07) although the reasons behind the choice may not always be discussed.

The latter, $M(<R)$, is a more fundamental lensing observable than $\kappa(R)$. Each set of multiple images constrains the mass within their radii $M(<R)$. The density profile $\kappa(R)$ within can only be constrained by multiple sets of multiple images at various redshifts (e.g., Saha & Read 2009). One should not worry about correlated errors in $M(<R)$ measurements. Instead one should worry about them in $\kappa(R)$ measurements.[13] These are generally ignored in the literature.

We plot $M(<R)$ from our SL modeling in Figure 8. We also plot the uncertainty in $M(<R)$ from our ensemble of models. Recall (Section 5.2) that each model in this ensemble uses a different subset of the multiple image systems. Thus, we are taking into account uncertainties related to the inclusion or exclusion of various systems.

The quantity $M(<R)$ is what lensing constrains best, especially $M(<R_E)$, the mass within the Einstein radius. Though our models vary, all give a very consistent amount of mass within $R_E \sim 47''$.

We derive an Einstein radius of $R_E = 47''.0 \pm 1''.2$ (143^{+3}_{-4} kpc) for a lensed source at $z_s = 2$. This value increases with redshift to $R_E \sim 52''$ for a source at $z_s = 7$. No cluster is perfectly symmetric, so the "correct" definition of Einstein radius is a bit ambiguous. As done elsewhere, we find that radius within which $\langle \kappa \rangle = 1$, the average mass surface density is equal to the critical lensing density (Equation (3)).

In Coe et al. (2008), we tested our method's ability to recover a mass distribution similar to A1689 given 93 multiple images of 19 lensed galaxies. Our recovered mass profile matched the input mass profile extremely well. In future work (Section 7), we will quantify our ability to recover input mass profiles and concentrations.

In Figure 9 (left), we verify that NFW fits to our $M(<R)$ are more tightly constrained than NFW fits to our $\kappa(R)$. In the right panel, we provide an illustrative explanation. There is a wider range of NFW profiles which fit $\kappa(R)$ well ($\chi^2 < 1$) than fit $M(<R)$ well.

Note that mass profiles of simulated galaxy clusters are often quoted in terms of their three-dimensional mass density $\rho(r)$. Lensing alone cannot measure $\rho(r)$ (although the addition of other data can constrain $\rho(r)$, as in Morandi et al. 2010). Reported measurements of $M(<R)$ in simulations would enable

---

[13] Consider the simple example of an Einstein ring observed at $R = R_E$. This ring constrains $M(<R_E)$ very well, but the density profile $\kappa(R)$ within is

degenerate (the "mass-sheet" degeneracy). Mass may be moved from $R \gtrsim 0$ to $R \lesssim R_E$ or vice versa, altering the $\kappa(R)$ profile slope while maintaining $M(<R_E)$ and reproducing the Einstein ring. Binned values of $\kappa(R)$ would clearly be correlated, though this is generally ignored in the literature. The constraints on $M(<R)$ are more fundamental.
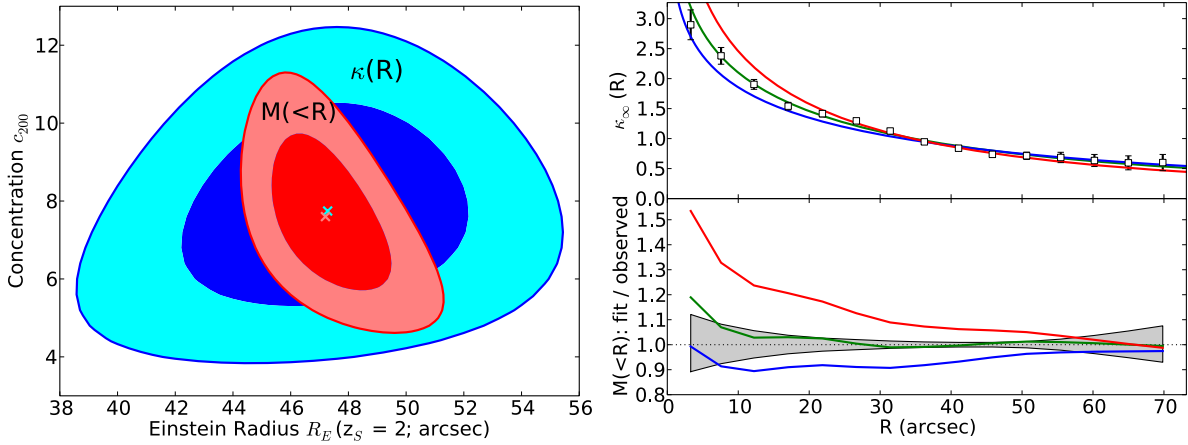
Figure 9. Fits to the enclosed mass $M(<R)$ provide tighter constraints than fits to the mass surface density $\kappa(R)$. We argue (Section 6.1) that the former is the more fundamental observable, and that binned $\kappa(R)$ (not $M(<R)$) have correlated uncertainties. Left: NFW fit confidence contours (1σ and 2σ) in the plane of Einstein radius $R_E(z_s = 2)$ and concentration c_{200}. Best-fit values are plotted as $\times$'s. (Note the NFW scale radius r_s is fixed by each (R_E, c) pair.) Right: illustration of why $M(<R)$ provides tighter constraints than $\kappa(R)$. Right top: best NFW fit (green) to the observed $\kappa(R)$ and two other fits with reduced $\chi^2 \approx 1$. While these are all reasonable fits to $\kappa(R)$, the red (blue) curve significantly overestimates (underestimates) the observed $M(<R)$ (gray; right bottom).

(A color version of this figure is available in the online journal.)
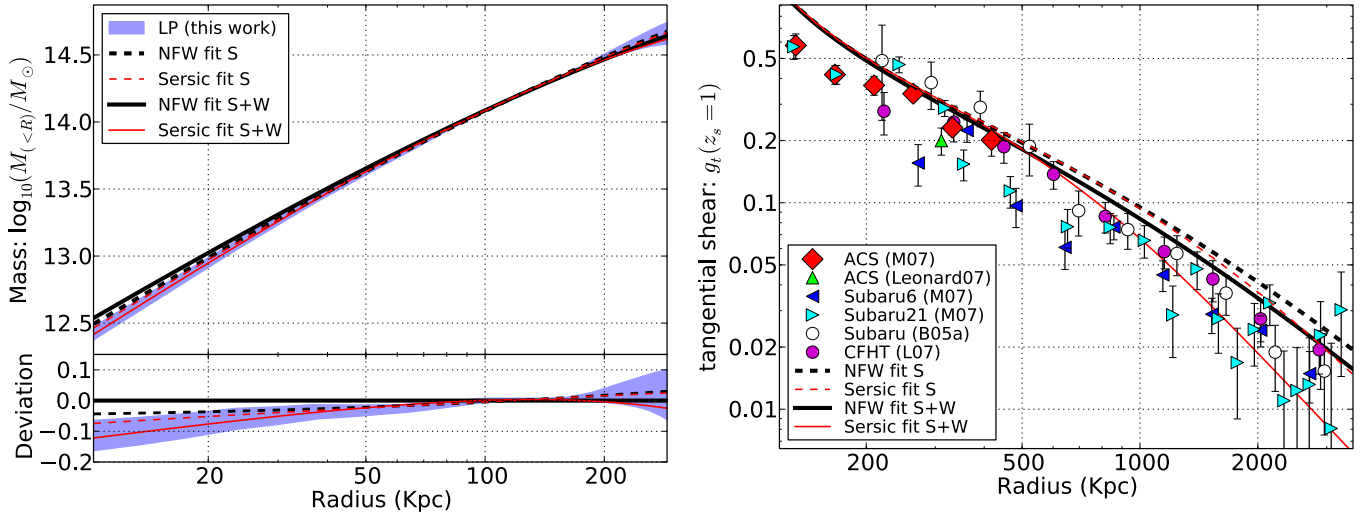
Figure 10. NFW and Sérsic profiles fit simultaneously to SL and WL data, inside and outside $R = 70'' \sim 220$ kpc, respectively. Also plotted are fits to the SL data alone. Left: the SL mass profile ($R < 70''$) derived in this work. Right: WL reduced tangential shears ($R > 70''$) measured in ACS (M07; Le07), Subaru (B05b; M07), and CFHT images (L07).

(A color version of this figure is available in the online journal.)

more direct comparison between lensing observations and simulations.

Along those lines, Broadhurst & Barkana (2008) compared observed measurements of Einstein radii R_E to those measured in simulations. The Einstein radius is a robust quantity which, for an axisymmetric potential, can be measured roughly by eye from the positions (and redshifts) of large arcs, then refined by model fitting. Measurement of R_E yields the equally robust $M(<R_E)$, as the average surface density within R_E must be equal to the critical lensing density $\Sigma_{\rm crit}$ (as a function of redshift). Our shift from analyzing $\kappa(R)$ to the more robust $M(<R)$ measurements (adopted by other authors as well) is a natural extension of the shift to robust R_E measurements by Broadhurst & Barkana (2008).

6.2. Simultaneous Fits to the SL and WL Data

Lensing-based constraints on mass–concentration are best derived from simultaneous SL + WL analyses. Together, SL

and WL probe a sufficient range of radius from the cluster center, capturing the profile turnover from $\rho \propto r^{-1}$ and $M(<R) \propto R^2$ near the core to $\rho \propto r^{-3}$ and $M(<R)$ rising slowly in the outskirts (see Coe 2010). Meneghetti et al. (2010b) quantify these statements, showing that SL + WL analyses of simulated clusters yield concentration measurements to $\sim 3\times$ greater precision than WL-only analyses (11% scatter versus 33% scatter) and $\sim 5\times$ greater precision than SL-only analyses (59% scatter).[14]

In Figure 10, we show NFW and Sérsic profiles fit *simultaneously* to SL $M(<R)$ from our model and WL shears measured in previous works (see below). Each profile, given a set of param-

---

[14] Meneghetti et al. (2010b) also find that concentrations derived from SL-only analyses are biased high by $\sim 60\%$ on average. They attribute this bias to their multi-component fit. They include an isothermal BCG component, but the BCG profile is actually steeper, and the parent halo must compensate with a higher concentration. Care must be taken in these comparisons however, as we and others measure concentration by fitting to the *total* mass profile (parent halo plus galaxy halos), not the DM halo alone.

COE ET AL.
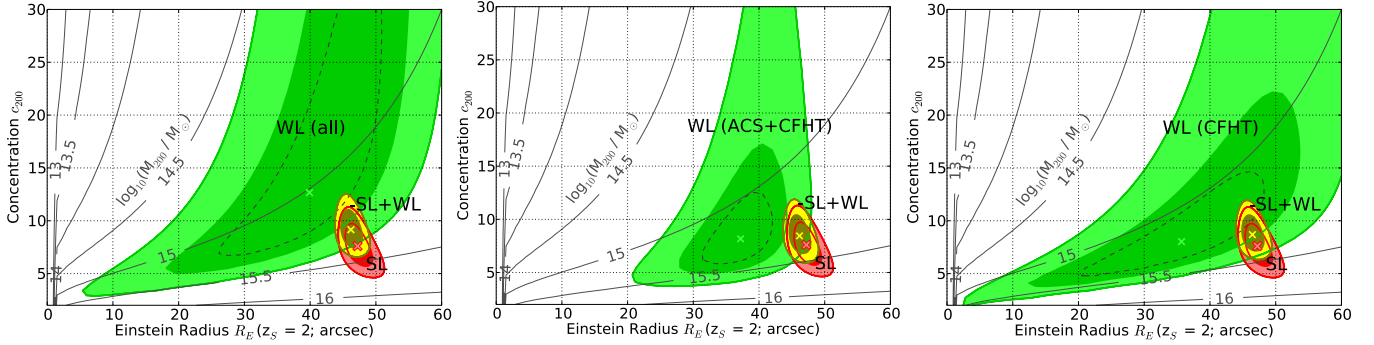
Figure 11. Constraints on Einstein radius R_E and concentration c_{200} from an NFW profile fit to the observed SL (red), WL (green), and both combined (yellow). Three sets of WL data are used—left: all; middle: CFHT (L07) and ACS (M07); right: CFHT (L07). Best fits are marked with ×'s. Confidence contours are 1σ (68%, $\Delta\chi^2 = 2.3$) and 2σ (95%, $\Delta\chi^2 = 6.17$). A black dashed line also indicates the one-dimensional 1σ WL contours ($\Delta\chi^2 = 1$), which give the 68% bounds if one parameter is marginalized over. Isocontours of M_{200} are overplotted.

(A color version of this figure is available in the online journal.)
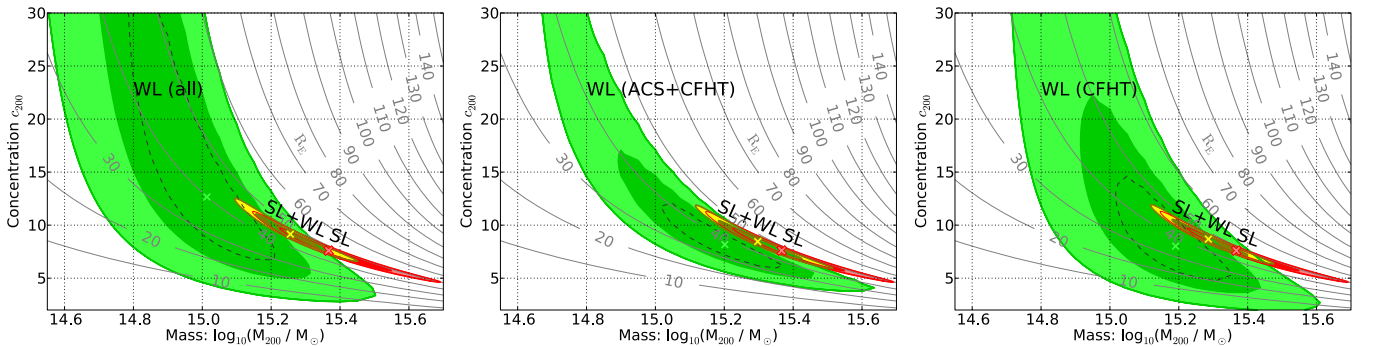
Figure 12. Same as Figure 11 but for mass within the virial radius M_{200} and NFW concentration c_{200}. Isocontours of R_E ($z_s = 2$; arcsec) are overplotted.

(A color version of this figure is available in the online journal.)

eters (e.g., r_s and c_{200}), predicts both $M(<R)$ and WL shears. For $R < 70''$ (∼220 kpc), we fit each profile to our SL $M(<R)$ model, and for $R > 70''$ we fit to the WL shears. We obtain an NFW fit of $r_s = 258^{+54}_{-40}$ kpc, $c_{200} = 9.2 \pm 1.2$ ($c_{vir} = 11.5^{+1.5}_{-1.4}$) and a best Sérsic fit of $R_e = 273.6$ kpc, $\kappa_e = 0.2939$, $n = 1.425$ ($b_n = 2.524$). Also plotted are fits to the SL data only.

Our NFW fits yield $M_{200} = 1.8^{+0.4}_{-0.3} \times 10^{15} \ M_\odot \ h_{70}^{-1}$ within $r_{200} = 2.4^{+0.1}_{-0.2}$ Mpc h_{70}^{-1} and $M_{vir} = 2.0^{+0.5}_{-0.3} \times 10^{15} \ M_\odot \ h_{70}^{-1}$ within the virial radius $r_{vir} = 3.0 \pm 0.2$ Mpc h_{70}^{-1}. By definition, the average overdensities within these regions are $\Delta_c = 200$ and 115, respectively, relative to the critical density to close the universe (see Appendix A).

We fit to an ensemble of WL data measured in ACS (Medezinski et al. 2007, hereafter M07; Leonard et al. 2007, hereafter Le07), Subaru (Broadhurst et al. 2005a, hereafter B05b; M07), and CFHT images (L07). We also experiment by fitting to various subsets of this data ensemble.

Figure 11 compares constraints on (R_E, c_{200}) for NFW fits to SL and WL combined using three different WL data sets. We consider the L07 CFHT data (right), these data combined with the M07 ACS data (middle), and all data (left). Figure 12 is similar but shows constraints on (M_{200}, c_{200}).

Our derived SL + WL parameters are not affected greatly by our choice of WL data subset. However, we note that inclusion of the Subaru WL measurements does increase the concentration slightly.

Note that B05b converted their shear measurements $\gamma(R)$ to mass measurements $\kappa(R)$ using their measurements of magnification $\mu(R)$ to break the mass-sheet degeneracy. For the purposes of fitting an NFW (or Sérsic) profile to the data, we prefer

to avoid this step which may introduce additional uncertainty. H06 use the more direct approach which we use here as well.

6.3. Comparison to Previous Work

In Figure 13, we compare our NFW fit parameters to published values from other similar studies: fits to SL, WL, or both simultaneously. These published values and more can also be found in Table 2.

Our concentration derived from SL alone ($c_{200} = 7.6 \pm 1.3$) is higher than that obtained in previous SL analyses ($c_{200} \sim 6$), though our values agree roughly within the 1σ uncertainties. In Figure 14, we compare our SL $M(<R)$ to that obtained by Halkola et al. (2006). Just inside the Einstein radius, our $M(<R)$ is steeper and claims a lower uncertainty. This budges the concentration value higher.

We have neglected to mask out substructure which can potentially be problematic for NFW fits (e.g., Hennawi et al. 2007). However, we note the main subclump which we might exclude is located between ∼150 and 200 kpc from the cluster center. Our mass excess relative to H06 is at smaller radius, between ∼100 and 150 kpc.

From our SL + WL fits, we find $c_{200} = 9.2 \pm 1.2$. This lies between the values of $c_{200} = 7.6^{+0.3}_{-0.5}$ found by H06 and $c_{200} = 10.8^{+1.2}_{-0.8}$ found by B05b. We note that our results are in good agreement with more recent analyses that have found values of $c_{200} \approx 10 \pm 0.7$ from SL + WL + number counts (Umetsu & Broadhurst 2008; Umetsu et al. 2009) and SL + WL + X-ray data (Lemze et al. 2008).

We note our uncertainty contours closely follow the $R_E = 47''.5$ isocontour of constant Einstein radius. The best-fit NFW
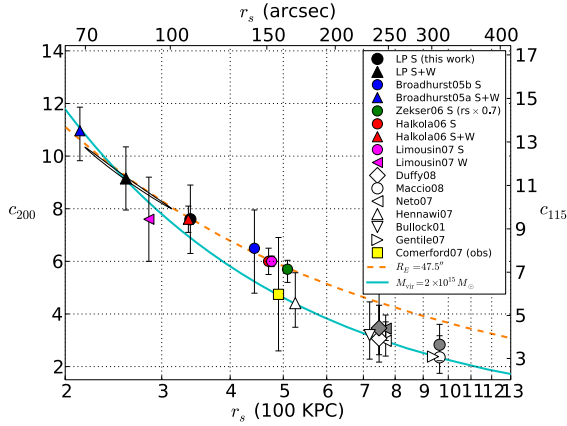
Figure 13. NFW fit parameters (r_s, c_{200} [c_{vir}]) found in this paper and in previous works compared to those predicted from simulations. Filled circles give best-fit SL parameters from B05, Z06, H06, L07, and ours $r_s = 338^{+105}_{-71}$ kpc, $c_{200} = 7.6 \pm 1.3$ ($c_{vir} = 9.6^{+1.7}_{-1.6}$). Filled upright triangles give SL + WL fits from B05b, H06, and ours $r_s = 258^{+54}_{-40}$ kpc, $c_{200} = 9.2 \pm 1.2$ ($c_{vir} = 11.5^{+1.5}_{-1.4}$). For clarity, error bars are plotted vertically, though they should actually all tightly follow the $R_E = 47\rlap{.}''5$ ($z_s = 2$) isocontour, as shown for our SL + WL fit. We also plot the WL fit obtained by L07. This fit, with $R_E = 30''$ ($z_s = 2$), is the only fit to fall far from the $R_E = 47\rlap{.}''5$ ($z_s = 2$) isocontour. (Again note the error bar is not properly oriented.) Along the isocontour $M_{200} = 2 \times 10^{15} M_\odot$ (our best-fit value), we have plotted concentrations observed in simulations (Bullock et al. 2001; Hennawi et al. 2007; Neto et al. 2007; Macciò et al. 2008; Duffy et al. 2008), including the original NFW prescription (Navarro et al. 1996) adapted to the present cosmology by Gentile et al. (2007). All assume a scaling of $c \propto (1+z)^{-1}$ except Duffy et al. (2008) which find roughly $c \propto (1+z)^{-0.45}$. Their shallower dependence on z happens to bring their lower values back in line with some earlier predictions. Filled symbols are plotted for relaxed subsets of the full samples. Again the error bars are plotted vertically, but here should follow the $M_{200} = 2 \times 10^{15} M_\odot$ isocontour. Finally, the mass–concentration relation observed in clusters (Comerford & Natarajan 2007) is plotted as the yellow square.

(A color version of this figure is available in the online journal.)
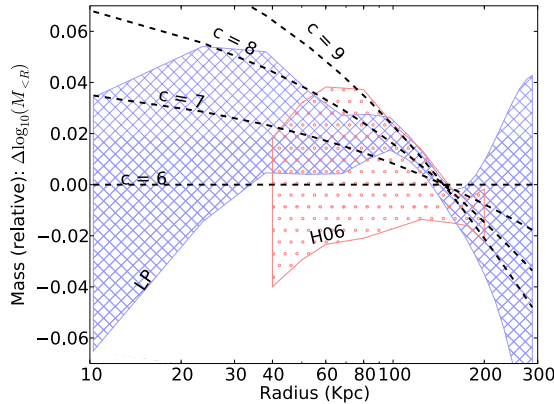
Figure 14. Comparison of our SL model $M(<R)$ to that of H06. Also plotted are four different NFW profiles with $c_{200} = 6$, 7, 8, and 9, all with the correct Einstein radius. All of the profiles are normalized to the $c_{200} = 6$ NFW profile. Our SL model has a higher concentration ($c_{200} = 7.6 \pm 1.3$) than that of H06 ($c_{200} = 6 \pm 0.5$).

(A color version of this figure is available in the online journal.)

parameters obtained in previous SL or SL + WL studies all fall along this line, as the Einstein radius is tightly constrained by SL.

6.4. Tension between the SL and WL Data?

In every SL + WL study published to date for A1689, including ours, the WL data prefer a higher concentration and steeper mass slope than the SL data (Figures 13 and 15). While we
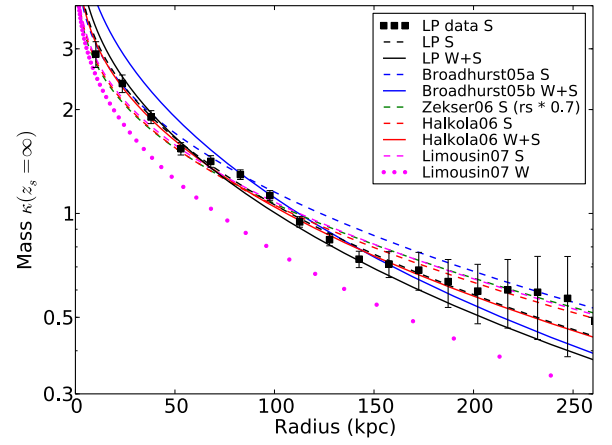
Figure 15. Our SL-derived mass density profile $\kappa(R)$ (black squares), along with our NFW profile fits and those published elsewhere. All fits which incorporate SL data (dashed: SL only; solid: SL + WL) provide reasonable fits to our SL data at most radii. The L07 WL-only NFW fit (dotted line) underpredicts the mass surface density at all radii plotted here.

(A color version of this figure is available in the online journal.)

have found a single NFW profile which provides a decent fit to both the SL and WL data, there is a slight tension between the two. While compatible at 1σ depending on the WL data set chosen (see Figure 11), the WL signal is a bit too low and/or falls off a bit too quickly relative to the SL data. Alternatively, the inner SL mass profile is a bit too shallow. We might suspect the WL signal has been diluted from contamination of the sample by unlensed (foreground or cluster) objects. However, M07 carefully considered and quantified dilution in their work.

We note that these deviations from NFW are qualitatively in accord with those proposed by Lapi & Cavaliere (2009), as found in their semianalytic modeling of cluster formation. This could prove interesting if similar variations are detected in many clusters. Slight deviations from NFW are not surprising in a single cluster, as simulated cluster profiles do exhibit intrinsic variations.

We note that L07 had claimed to resolve the discrepancy of SL versus WL concentrations. They fit NFW profiles separately to their SL and WL data, finding concentration parameters of $c_{200} = 6.0 \pm 0.6$ (3σ) and $c_{200} = 7.6 \pm 1.6$ (1σ), respectively. As the error bars overlap, they claimed agreement. However, as we showed in Figure 11, SL-only and WL-only NFW fits may yield similar concentration values but very different Einstein radii. L07's best fit to the WL data yields $R_E \approx 30''$ ($z_s = 2$), significantly lower than the value $R_E \approx 47''$ tightly constrained by SL. This fit underpredicts mass at all radii within the Einstein radius (Figure 13). L07 did not attempt to provide a single profile which provides an acceptable fit to both the SL and WL data simultaneously.

6.5. Comparison to Predictions

Our results support findings that A1689 has a higher concentration than predicted by simulations for a cluster of its mass. According to Duffy et al. (2008), a cluster such as A1689 with $M_{200} \approx 2 \times 10^{15} M_\odot$ at $z = 0.186$ should have $c_{200} = 3.0^{+1.3}_{-0.9}$ ($c_{vir} = 3.9^{+1.6}_{-1.1}$). Relaxed clusters are more symmetric yielding better fits to NFW profiles and $\sim$20% higher concentrations for clusters of this mass: $c_{200} = 3.4^{+1.4}_{-1.0}$ ($c_{vir} = 4.4^{+1.8}_{-1.3}$). Estimates from Macciò et al. (2008) are similar ($\sim$10% lower) though the normal $c \propto (1+z)^{-1}$ scaling relation (Bullock et al. 2001) drags

the predictions down another $\sim$10%. Duffy et al. (2008) instead find roughly $c_{200} \propto (1+z)^{-0.45}$ and $c_{\rm vir} \propto (1+z)^{-0.70}$.

Predictions from Bullock et al. (2001), Gentile et al. (2007), and Neto et al. (2007, who analyzed the Millennium simulation) are also fairly similar to the Duffy et al. (2008) predictions despite concerns about each. The Millennium simulation used a WMAP1 cosmology (Spergel et al. 2003) including $\sigma_8 = 0.9$. Duffy et al. (2008) and Macciò et al. (2008) found this results in concentrations $\sim$15% higher than their WMAP5 (Komatsu et al. 2009) input $\sigma_8 = 0.796$.[15] The Bullock et al. (2001) simulations used $\sigma_8 = 1.0$ and did not produce halos as massive as A1689. Zhao et al. (2003) cite the dangers of extrapolating these results to higher mass. Gentile et al. (2007) is a reformulation of the original Navarro et al. (1996) prescription to WMAP3 (Spergel et al. 2007). Those early simulations were lower resolution and produced only 19 halos (compared to $\sim$1000 and $\sim$10,000 for Duffy et al. 2008 and Macciò et al. 2008, respectively).

Hennawi et al. (2007) measure significantly larger concentrations in their simulations. For A1689, they predict $c_{200} = 4.4^{+1.2}_{-0.9}$, $\sim$50% larger than predicted by Duffy et al. (2008). Their use of $\sigma_8 = 0.95$ probably only results in concentrations inflated by $\sim$20%. The remaining disagreement may be a result of their halo density fitting procedure which they claim is better for comparison with lensing measurements.

All of these predictions (detailed further in Coe 2010) are plotted in Figure 13. The predictions are all significantly lower than our SL + WL-derived $c_{200} = 9.2 \pm 1.2$.

Clusters selected with a lensing bias may have measured concentrations biased high by $\sim$34% Hennawi et al. (2007), $\sim$50% Oguri & Blandford (2009), or even $\sim$100% Meneghetti et al. (2010a), on average. This results from a combination of higher intrinsic (three-dimensional) concentrations and additional mass along the line of sight (either due to cluster elongation or otherwise) resulting in higher projected (two-dimensional) concentrations. The $c_{200} = 4.4^{+1.2}_{-0.9}$ predicted by Hennawi et al. (2007) plus a $\sim$100% bias might begin to explain measurements of $c_{200} \sim 9$. However, such extremely high biases are expected only for less massive clusters. Even accounting for such biases, the high concentration of A1689 seems unlikely given the results from ΛCDM simulations (Broadhurst & Barkana 2008; Oguri & Blandford 2009).

There are fewer published fits of Sérsic profiles to simulated cluster halos. We do note that Merritt et al. (2005) found $n = 2.38 \pm 0.25$ for their cluster sample.[16] Our best-fit $n = 1.425$ is much lower giving our density profile a more rapidly varying slope. This allows it to fit both the SL profile and the low WL signal measured by some authors at large radius. We have not experimented with fitting Sérsic profiles to various subsets of the WL data.

Recently, the Einasto profile has gained popularity over the Sérsic profile (e.g., Navarro et al. 2010). The two have similar forms, but the former gives density $\rho(r)$ as a function of three-dimensional radius, while the latter gives surface density $\Sigma(R)$ as a function of projected two-dimensional radius. The former was found (Merritt et al. 2006) to provide better fits to halos of a wide range of masses, though the latter performed slightly better specifically for cluster halos (and only slightly worse

for galaxy halos). Mass–concentration relations derived from Einasto profile fits have been published by Duffy et al. (2008), Gao et al. (2008), and Hayashi & White (2008). These fits yield slightly ($<$20%) different concentrations than NFW fits (Coe 2010). We do not explore Einasto profile fits here.

The Sérsic profile remains intriguing for the direct comparisons which can be made (Merritt et al. 2005) to many published Sérsic fits to galaxy luminosity profiles (although this may just be coincidental Dhar & Williams 2010). We also note the possibility of using well established software such as GALFIT (Peng et al. 2002) to derive Sérsic parameters for surface density mass maps.

7. FUTURE WORK

In this paper, we have focused on measurement of the radial mass profile of A1689. However, a key strength of LensPerfect is its ability to map massive substructure without assuming LTM. In future work, we will verify in detail our ability to resolve halo subclumps as well as measure their masses. The latter proves difficult (both in observed and simulated halos) as the subhalo masses must be disentangled cleanly from the greater parent halo (e.g., Natarajan et al. 2009; Jullo & Kneib 2009).

One novel method developed recently by Powell et al. (2009) demonstrates the ability to detect subclumps in a two-dimensional mass map down to 10^{13} or even 10^{12} $M_\odot$ and measure their masses to within a factor of 2. By weighing subhalos associated with cluster galaxies, we may provide evidence for galaxy halo stripping in individual galaxies. This would provide an excellent complement to studies which have measured stripping statistically, averaged over many galaxy halos (Natarajan et al. 1998, 2002, 2009; Gavazzi et al. 2004; Limousin et al. 2007a, 2009; Halkola et al. 2007).

Williams & Saha (2004) and Saha et al. (2007) have experimented with several methods to identify substructure in their non-LTM (PixeLens) mass models. From the two-dimensional mass density map $\kappa(\vec{\theta})$, they have subtracted each of the following: the average $\kappa(R)$ in that radial bin; $\kappa(\vec{\theta})$ 180° across (directly opposite with respect to the center), or the best-fitting NFW profile. In Saha et al. (2007), they show that the observed substructure (extended "meso-structure") appears to correlate with the luminous galaxies. Alard (2008) discusses the possibility of quantifying the amounts of substructure found in their multipole models.

In future work, we will develop algorithms to thoroughly explore the range of model solutions which perfectly reproduce all observed multiple image positions. This method must take care not to remain trapped in a local minimum near our "best" solution. Also, we must correctly account for the larger uncertainties in voids between the multiple images.

In Coe et al. (2008), we discussed our ability to mold the mass map by adding extra artificial constraints. These modified mass models would successfully reproduce all of the input data plus the artificial constraints. These added constraints squeeze the mass model, tweaking the positions of subclumps or increasing the concentration of mass in the desired regions. We must explore such solutions to accurately account for all uncertainties. We may also mold our mass models in attempts to force mass to follow light more closely. We might construct that mass model which follows light best, as in, for example, Saha & Williams (1997).

Ultimately, a hybrid approach combining non-LTM and flexible-LTM components may prove ideal. A prior of LATM

---

[15] This value is in excellent agreement with the *WMAP* seven year maximum likelihood value $\sigma_8 = 0.803$ (Komatsu et al. 2010).

[16] Alternatively, fitting a deprojected Sérsic profile to the three-dimensional spatial density $\rho(r)$, Merritt et al. (2005) and Merritt et al. (2006) found $n_d = 2.99 \pm 0.49$ and $n_d = 2.89 \pm 0.49$, respectively. The deprojection they used (Prugniel & Simien 1997) is approximate and thus does not yield exactly the same n as fitting directly to the surface density.

could be assumed. This ideal method would include a parent halo, galaxy components, and line-of-sight structure, all with *sufficient flexibility*. Each galaxy component might be allowed to vary individually in *M/L*, radial scale, truncation radius, and perhaps position. Different forms may even be explored: truncated isothermal ellipsoid versus NFW, for example. The parent halo should be very flexible (a multi-scale grid perhaps) to allow for the asymmetries induced as galaxies infall and their stripped mass is strewn about the cluster. Additional mass planes behind the lens should also be modeled.

Future deeper observations of galaxy clusters such as A1689 may reveal hundreds of multiple images. This wealth of constraints will allow truly high-definition mass models, which clearly resolve individual galaxy halos and perhaps dark subhalos as well (Coe 2009). As more multiple images are revealed and greater details are obtained, line-of-sight structure will need to be taken into account. While seemingly a nuisance, this raises the prospect of SL tomography—the mapping of mass in multiple lens planes.

Over the next two to three years, we are looking forward to new *HST* images from the CLASH Multi-Cycle Treasury Program. As mentioned in Section 1, this program will image 25 clusters to a depth of 20 orbits each, equal to the depth of the A1689 images studied here. Analysis of these ACS and WFC3 images along with supporting data will yield measurements of mass–concentration for a sizable sample of clusters, selected free of lensing bias. By comparing these values to the concentrations of simulated halos, we expect to either show agreement or detect average deviations as small as 15% with 99% confidence.

8. SUMMARY

We have presented an SL mass model of A1689 which resolves structures down to an estimated ∼25 kpc on average within the central 400 kpc diameter without assuming LTM. If confirmed, this would be the highest resolution mass map of any galaxy cluster to date. The most luminous galaxies appear to trace the mass distribution fairly well but with some deviations which may prove interesting, pending verification. Our mass model perfectly reproduces the observed positions of 168 multiple images of 55 knots within 135 images of 42 galaxies. Included are 20 new candidate multiple images of eight galaxies which we have identified in this work. We have also tweaked some of the identifications from previous works, discarding three suspect central images and adding one new one.

Compiling published WL measurements from ACS, Subaru, and CFHT images, we find that a single mass profile, either NFW or Sérsic, is able to provide a decent fit simultaneously to both the observed weak and SL. However, there remains a slight tension in that the WL data prefer higher concentrations than the strong lensing data.

Based on simultaneous fitting of the SL and WL data, we measure an NFW central mass–concentration of $c_{200} = 9.2 \pm 1.2$ ($c_{\mathrm{vir}} = 11.5^{+1.5}_{-1.4}$). Thus, we concur with previous claims that the mass profile of A1689 appears to be more centrally concentrated than clusters of similar mass ($M_{200} \sim 2 \times 10^{15} M_{\odot} h_{70}^{-1} = 1.4 \times 10^{15} M_{\odot} h^{-1}$) formed in CDM simulations ($c_{200} \sim 3$; $c_{\mathrm{vir}} \sim 4$).

The large measured concentrations of A1689 and other clusters are difficult (though possible) to explain solely by selection bias and projection effects including triaxiality (e.g., Broadhurst et al. 2008; Oguri et al. 2009; Corless et al. 2009). A more definitive comparison based on 25 well-studied clusters

free of lensing bias is expected from the CLASH Hubble Multi-Cycle Treasury Program (Sections 1 and 7).

In future work, we will perform further simulations and verify our ability to not only resolve substructure but measure the masses of these halo subclumps. Backed by these tests, future analyses of our substructure maps should yield further evidence for galaxy halo stripping in cluster environments, test the degree to which LTM, and perhaps even lead to detection of dark subhalos, should they exist.

APPENDIX A

DARK MATTER HALO MASS PROFILES

Clusters formed in simulations have mass profiles generally well described by NFW (Navarro et al. 1996) or Einasto/Sérsic (Navarro et al. 2004) profiles (e.g., Navarro et al. 2010). The latter were found to yield superior fits to simulated halos (Navarro et al. 2004, 2010; Merritt et al. 2005, 2006). Details on these fitting forms can be found in Coe (2010).

The NFW profile gives mass density as a function of radius in three dimensions:

$$\rho(r) = \frac{\rho_s}{(r/r_s)(1 + r/r_s)^2}. \tag{A1}$$

The logarithmic slope increases from -1 at the core to -3 in the outskirts. The NFW concentration parameter is given as $c = r_{\mathrm{vir}}/r_s$. By definition, the average density within the virial radius r_{vir} is $\Delta_c \approx 115$ times $\rho_{\mathrm{crit}} = 3H^2(z)/(8\pi G)$ for a collapsed virialized sphere at $z = 0.186$, as evaluated according to formulae given by Nakamura & Suto (1997). For historical reasons, $\Delta_c \approx 200$ is often used, so we report concentration values for both overdensities. Conversion between the two is given by $c_{115} \approx 1.234 c_{200} + 0.172$. Lensing properties of the NFW profile can be found in Golse & Kneib (2002).

The Sérsic (1968) profile has a continuously varying slope that asymptotes toward zero at very small radius. Its use as a mass profile is described by Graham & Driver (2005) and Terzić & Graham (2005) with lensing properties calculated by Cardone (2004) and Elíasdóttir & Möller (2007). These details are summarized in Coe (2010). Our Sérsic profile of *projected* mass is given as

$$\Sigma(R) = \Sigma_e \exp\left\{-b_n\left[\left(\frac{R}{R_e}\right)^{1/n} - 1\right]\right\}. \tag{A2}$$

There are three free parameters: Σ_e, R_e, and n, with b_n being a function of n. This profile was found (Navarro et al. 2004; Merritt et al. 2005, 2006) to yield better fits to a wide range of simulated dark matter halos than did the generalized NFW profile (Zhao 1996; Wyithe et al. 2001), which has an equal number (3) of free parameters, including the central slope.
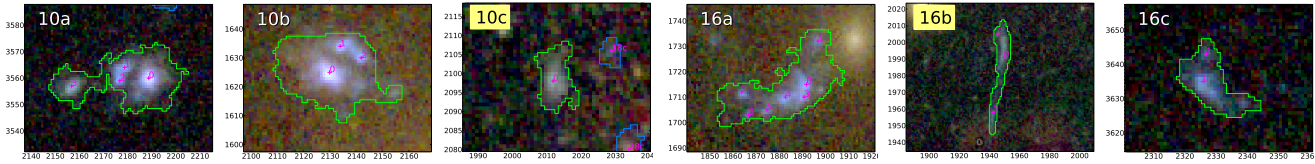
Figure 16. Multiple images in A1689. For each image, identified knots are labeled with numbers and crosses. Green lines are isophotal apertures, altered where necessary. Yellow boxes outlining the IDs indicate color image stamps that were produced from our galaxy-subtracted images. All other color stamps are taken from the STScI $g'r'z'$ color image. Coordinates in pixels are given along the axes. Each pixel measures 0″.05 across.
(A color version of this figure and the complete figure set (135 images) are available in the online journal.)
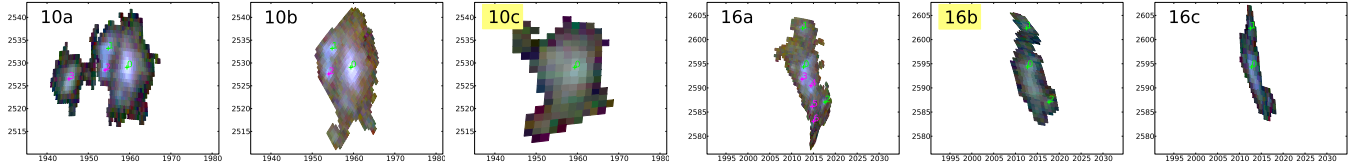
Figure 17. Multiple images delensed to the source plane. Knots are labeled as in Figure 16, but now constrained knots are colored green and unconstrained knots are colored pink. Within each system, all of the constrained knots align exactly among the delensed images. Unconstrained knots are generally well aligned but not always. Panels are plotted to the same scale within each system. Yellow boxes outlining the IDs indicate color image stamps that were produced from our galaxy-subtracted images. All other color stamps are taken from the STScI $g'r'z'$ color image. Coordinates in pixels are given along the axes. Each pixel measures 0″.05 across.
(A color version of this figure and the complete figure set (135 images) are available in the online journal.)

A distinction has been made between the Sérsic profile described above and the Einasto profile. The latter has a similar form but is defined as a function of three-dimensional density $\rho(r)$ rather than projected surface density $\Sigma(R) = \kappa(R)\Sigma_{\text{crit}}$. Performance of the two forms is similar with the Sérsic profile providing a slightly better fit to cluster halos (Merritt et al. 2006). These and other mass profiles are described in more detail in Coe (2010).

APPENDIX B

MULTIPLE IMAGES

In this section, we display color images of the multiple images used in this work. Figure 16 displays the images as they appear and Figure 17 displays the same images delensed, as they would appear if A1689 did not exist (according to our best mass model). The 55 constrained positions are labeled in green in Figure 17. These delensed positions match perfectly among each set of multiple images. We have identified other knots, labeled in pink, which we have not constrained. We have doubts about these identifications (including a case or two in which it appears that we were obviously mistaken).

Examples of the image stamps are given here. The remaining images (for all 42 image systems) can be found in the online version.

REFERENCES

Q4
Q5

Alard, C. 2008, MNRAS, 388, 375
Alard, C. 2009, A&A, 506, 609
Q6 Alard, C. 2010, arXiv:1005.2540
Andersson, K. E., & Madejski, G. M. 2004, ApJ, 607, 190
Balogh, M. L., Couch, W. J., Smail, I., Bower, R. G., & Glazebrook, K. 2002, MNRAS, 335, 10
Bardeau, S., Kneib, J., Czoske, O., Soucail, G., Smail, I., Ebeling, H., & Smith, G. P. 2005, A&A, 434, 433
Bardeau, S., Soucail, G., Kneib, J., Czoske, O., Ebeling, H., Hudelot, P., Smail, I., & Smith, G. P. 2007, A&A, 470, 449
Barkana, R., & Loeb, A. 2009, arXiv:0907.1102
Benítez, N. 2000, ApJ, 536, 571
Benítez, N., et al. 2004, ApJS, 150, 1
Bertin, E., & Arnouts, S. 1996, A&AS, 117, 393

Blakeslee, J. P., Anderson, K. R., Meurer, G. R., Benítez, N., & Magee, D. 2003, in ASP Conf. Ser. 295, Astronomical Data Analysis Software and Systems XII, ed. H. E. Payne (San Francisco, CA: ASP) 257
Bradač, M., et al. 2006, ApJ, 652, 937
Bradley, L. D., et al. 2008, ApJ, 678, 647
Broadhurst, T. J., & Barkana, R. 2008, MNRAS, 390, 1647
Broadhurst, T., Takada, M., Umetsu, K., Kong, X., Arimoto, N., Chiba, M., & Futamase, T. 2005a, ApJ, 619, L143
Broadhurst, T., Umetsu, K., Medezinski, E., Oguri, M., & Rephaeli, Y. 2008, ApJ, 685, L9
Broadhurst, T., et al. 2005b, ApJ, 621, 53
Bullock, J. S., Kolatt, T. S., Sigad, Y., Somerville, R. S., Kravtsov, A. V., Klypin, A. A., Primack, J. R., & Dekel, A. 2001, MNRAS, 321, 559
Bunker, A. J., Moustakas, L. A., & Davis, M. 2000, ApJ, 531, 95
Cardone, V. F. 2004, A&A, 415, 839
Clowe, D. 2003, in ASP Conf. Ser. 301, ed. S. Bowyer & C.-Y. Hwang (San Francisco, CA: ASP) 271
Clowe, D., Bradač, M., Gonzalez, A. H., Markevitch, M., Randall, S. W., Jones, C., & Zaritsky, D. 2006, ApJ, 648, L109
Clowe, D., & Schneider, P. 2001, A&A, 379, 384
Coe, D. 2009, Astro2010: The Astronomy and Astrophysics Decadal Survey, 51
Coe, D. 2010, arXiv:1005.0411
Coe, D., Benítez, N., Sánchez, S. F., Jee, M., Bouwens, R., & Ford, H. 2006, AJ, 132, 926
Coe, D., Fuselier, E., Benítez, N., Broadhurst, T., Frye, B., & Ford, H. 2008, ApJ, 681, 814
Coe, D., & Moustakas, L. A. 2009, ApJ, 706, 45
Coles, J. 2008, ApJ, 679, 17
Comerford, J. M., & Natarajan, P. 2007, MNRAS, 379, 190
Congdon, A. B., & Keeton, C. R. 2005, MNRAS, 364, 1459
Corless, V. L., King, L. J., & Clowe, D. 2009, MNRAS, 393, 1235
Deb, S., Goldberg, D. M., Heymans, C., & Morandi, A. 2009, arXiv:0912.4260
Dhar, B. K., & Williams, L. L. R. 2010, MNRAS, 480
Diego, J. M., Protopapas, P., Sandvik, H. B., & Tegmark, M. 2005a, MNRAS, 360, 477
Diego, J. M., Sandvik, H. B., Protopapas, P., Tegmark, M., Benítez, N., & Broadhurst, T. 2005b, MNRAS, 362, 1247
Diego, J. M., Tegmark, M., Protopapas, P., & Sandvik, H. B. 2007, MNRAS, 375, 958
Duc, P.-A., et al. 2002, A&A, 382, 60
Duffy, A. R., Schaye, J., Kay, S. T., & Dalla Vecchia, C. 2008, MNRAS, 390, L64
Duffy, A. R., Schaye, J., Kay, S. T., Dalla Vecchia, C., Battye, R. A., & Booth, C. M. 2010, arXiv:1001.3447
Einstein, A. 1916, Ann. Phys., 354, 769
Eisenhardt, P. R. M., et al. 2008, ApJ, 684, 905
Elíasdóttir, Á., & Möller, O. 2007, J. Cosmol. Astropart. Phys., 7, 6
Elíasdóttir, Á., et al. 2007, arXiv:0710.5636
Evans, N. W., & Witt, H. J. 2003, MNRAS, 345, 1351

Fedeli, C., & Bartelmann, M. 2007, A&A, 461, 49
Feng, J. L., Kaplinghat, M., Tu, H., & Yu, H. 2009, J. Cosmol. Astropart. Phys., 7, 4
Fort, B., Mellier, Y., & Dantel-Fort, M. 1997, A&A, 321, 353
Francis, M. J., Lewis, G. F., & Linder, E. V. 2009, MNRAS, 394, 605
Frye, B., Broadhurst, T., & Benítez, N. 2002, ApJ, 568, 558
Frye, B. L., et al. 2007, ApJ, 665, 921
Frye, B. L., et al. 2008, ApJ, 685, L5
Fukugita, M., Futamase, T., Kasai, M., & Turner, E. L. 1992, ApJ, 393, 3
Fusco-Femiano, R., Cavaliere, A., & Lapi, A. 2009, ApJ, 705, 1019
Fuselier, E. J. 2006, PhD thesis, Texas A&M Univ.
Fuselier, E. 2007, Adv. Comput. Math.
Gao, L., Navarro, J. F., Cole, S., Frenk, C. S., White, S. D. M., Springel, V., Jenkins, A., & Neto, A. F. 2008, MNRAS, 387, 536
Gavazzi, R., Mellier, Y., Fort, B., Cuillandre, J., & Dantel-Fort, M. 2004, A&A, 422, 407
Gentile, G., Tonini, C., & Salucci, P. 2007, A&A, 467, 925
Gilmore, J., & Natarajan, P. 2009, MNRAS, 396, 354
Golse, G., & Kneib, J.-P. 2002, A&A, 390, 821
Graham, A. W., & Driver, S. P. 2005, PASA, 22, 118
Grossi, M., & Springel, V. 2009, MNRAS, 394, 1559
Halkola, A., Seitz, S., & Pannella, M. 2006, MNRAS, 372, 1425
Halkola, A., Seitz, S., & Pannella, M. 2007, ApJ, 656, 739
Hayashi, E., & White, S. D. M. 2008, MNRAS, 388, 2
Hennawi, J. F., Dalal, N., Bode, P., & Ostriker, J. P. 2007, ApJ, 654, 714
Heymans, C., et al. 2008, MNRAS, 385, 1431
Hildebrandt, H., Wolf, C., & Benítez, N. 2008, A&A, 480, 703
Hogg, D. W. 1999, arXiv:astro-ph/9905116
Huang, X., et al. 2009, ApJ, 707, L12
Jee, M. J., et al. 2007, ApJ, 661, 728
Jee, M. J., et al. 2009, ApJ, 704, 672
Jullo, E., & Kneib, J. 2009, MNRAS, 395, 1319
Kawaharada, M., et al. 2010, ApJ, 714, 423
King, L. J., Clowe, D. I., Lidman, C., Schneider, P., Erben, T., Kneib, J., & Meylan, G. 2002a, A&A, 385, L5
King, L. J., Clowe, D. I., & Schneider, P. 2002b, A&A, 383, 118
Komatsu, E., et al. 2009, ApJS, 180, 330
Komatsu, E., et al. 2010, arXiv:1001.4538
Lapi, A., & Cavaliere, A. 2009, ApJ, 695, L125
Lemze, D., Barkana, R., Broadhurst, T. J., & Rephaeli, Y. 2008, MNRAS, 386, 1092
Lemze, D., Broadhurst, T., Rephaeli, Y., Barkana, R., & Umetsu, K. 2009, ApJ, 701, 1336
Leonard, A., Goldberg, D. M., Haaga, J. L., & Massey, R. 2007, ApJ, 666, 51
Liesenborgs, J., De Rijcke, S., & Dejonghe, H. 2006, MNRAS, 367, 1209
Liesenborgs, J., de Rijcke, S., Dejonghe, H., & Bekaert, P. 2007, MNRAS, 380, 1729
Liesenborgs, J., de Rijcke, S., Dejonghe, H., & Bekaert, P. 2009, MNRAS, 397, 341
Limousin, M., Kneib, J. P., Bardeau, S., Natarajan, P., Czoske, O., Smail, I., Ebeling, H., & Smith, G. P. 2007a, A&A, 461, 881
Limousin, M., Sommer-Larsen, J., Natarajan, P., & Milvang-Jensen, B. 2009, ApJ, 696, 1771
Limousin, M., et al. 2007b, ApJ, 668, 643
Macciò, A. V., Dutton, A. A., & van den Bosch, F. C. 2008, MNRAS, 391, 1940
Mahdavi, A., Hoekstra, H., Babul, A., Balam, D. D., & Capak, P. L. 2007, ApJ, 668, 806
Mantz, A., Allen, S. W., Rapetti, D., & Ebeling, H. 2009, arXiv:0909.3098
Markevitch, M., Gonzalez, A. H., Clowe, D., Vikhlinin, A., Forman, W., Jones, C., Murray, S., & Tucker, W. 2004, ApJ, 606, 819
Mead, J. M. G., King, L. J., Sijacki, D., Leonard, A., Puchwein, E., & McCarthy, I. G. 2010, arXiv:1001.2281
Medezinski, E., et al. 2007, ApJ, 663, 717
Meneghetti, M., Fedeli, C., Pace, F., Gottloeber, S., & Yepes, G. 2010a, arXiv:1003.4544
Meneghetti, M., Rasia, E., Merten, J., Bellagamba, F., Ettori, S., Mazzotta, P., Dolag, K., & Marri, S. 2010b, A&A, 514, A93
Merritt, D., Graham, A. W., Moore, B., Diemand, J., & Terzić, B. 2006, AJ, 132, 2685
Merritt, D., Navarro, J. F., Ludlow, A., & Jenkins, A. 2005, ApJ, 624, L85
Merten, J., Cacciato, M., Meneghetti, M., Mignone, C., & Bartelmann, M. 2009, A&A, 500, 681

Mieske, S., Infante, L., Hilker, M., Hertling, G., Blakeslee, J. P., Benítez, N., Ford, H., & Zekser, K. 2005, A&A, 430, L25
Mieske, S., et al. 2004, AJ, 128, 1529
Miralda-Escude, J., & Babul, A. 1995, ApJ, 449, 18
Morandi, A., Pedersen, K., & Limousin, M. 2010, arXiv:1001.1656
Nakamura, T. T., & Suto, Y. 1997, Prog. Theor. Phys., 97, 49
Natarajan, P., Kneib, J., & Smail, I. 2002, ApJ, 580, L11
Natarajan, P., Kneib, J., Smail, I., & Ellis, R. S. 1998, ApJ, 499, 600
Natarajan, P., Kneib, J., Smail, I., Treu, T., Ellis, R., Moran, S., Limousin, M., & Czoske, O. 2009, ApJ, 693, 970
Navarro, J. F., Frenk, C. S., & White, S. D. M. 1996, ApJ, 462, 563
Navarro, J. F., et al. 2004, MNRAS, 349, 1039
Navarro, J. F., et al. 2010, MNRAS, 402, 21
Neto, A. F., et al. 2007, MNRAS, 381, 1450
Newman, A. B., Treu, T., Ellis, R. S., Sand, D. J., Richard, J., Marshall, P. J., Capak, P., & Miyazaki, S. 2009, ApJ, 706, 1078
Oguri, M., & Blandford, R. D. 2009, MNRAS, 392, 930
Oguri, M., Takada, M., Umetsu, K., & Broadhurst, T. 2005, ApJ, 632, 841
Oguri, M., et al. 2009, ApJ, 699, 1038
Papovich, C., et al. 2010, ApJ, 716, 1503
Peng, E., Andersson, K., Bautz, M. W., & Garmire, G. P. 2009, ApJ, 701, 1283
Peng, C. Y., Ho, L. C., Impey, C. D., & Rix, H.-W. 2002, AJ, 124, 266
Powell, L. C., Kay, S. T., & Babul, A. 2009, MNRAS, 400, 705
Prugniel, P., & Simien, F. 1997, A&A, 321, 111
Randall, S. W., Markevitch, M., Clowe, D., Gonzalez, A. H., & Bradač, M. 2008, ApJ, 679, 1173
Richard, J., Pei, L., Limousin, M., Jullo, E., & Kneib, J. P. 2009, A&A, 498, 37
Richard, J., Stark, D. P., Ellis, R. S., George, M. R., Egami, E., Kneib, J., & Smith, G. P. 2008, ApJ, 685, 705
Richard, J., et al. 2010, MNRAS, 404, 325
Riemer-Sørensen, S., Paraficz, D., Ferreira, D. D. M., Pedersen, K., Limousin, M., & Dahle, H. 2009, ApJ, 693, 1570
Rozo, E., et al. 2010, ApJ, 708, 645
Sadeh, S., & Rephaeli, Y. 2008, MNRAS, 388, 1759
Saha, P., & Read, J. I. 2009, ApJ, 690, 154
Saha, P., Read, J. I., & Williams, L. L. R. 2006, ApJ, 652, L5
Saha, P., & Williams, L. L. R. 1997, MNRAS, 292, 148
Saha, P., & Williams, L. L. R. 2004, AJ, 127, 2604
Saha, P., Williams, L. L. R., & Ferreras, I. 2007, ApJ, 663, 29
Sand, D. J., Treu, T., Ellis, R. S., Smith, G. P., & Kneib, J. 2008, ApJ, 674, 711
Schwope, A. D., et al. 2010, A&A, 513, L10
Sereno, M., Jetzer, P., & Lubini, M. 2010, MNRAS, 403, 2077
Sérsic, J. L. 1968, in Atlas de galaxias australes, (Cordoba, Argentina: Observatorio Astronomico)
Spergel, D. N., et al. 2003, ApJS, 148, 175
Spergel, D. N., et al. 2007, ApJS, 170, 377
Taylor, A. N., Dye, S., Broadhurst, T. J., Benitez, N., & van Kampen, E. 1998, ApJ, 501, 539
Teague, P. F., Carter, D., & Gray, P. M. 1990, ApJS, 72, 715
Terzić, B., & Graham, A. W. 2005, MNRAS, 362, 197
Tyson, J. A., Kochanski, G. P., & dell'Antonio, I. P. 1998, ApJ, 498, L107
Tyson, J. A., Wenk, R. A., & Valdes, F. 1990, ApJ, 349, L1
Umetsu, K., & Broadhurst, T. 2008, ApJ, 684, 177
Umetsu, K., et al. 2009, ApJ, 694, 1643
Vegetti, S., Koopmans, L. V. E., Bolton, A., Treu, T., & Gavazzi, R. 2009, arXiv:0910.0760
Vikhlinin, A., et al. 2009, ApJ, 692, 1060
Wambsganss, J. 1998, Living Rev. Relativ., 1
Williams, L. L. R., & Saha, P. 2004, AJ, 128, 2631
Wyithe, J. S. B., Turner, E. L., & Spergel, D. N. 2001, ApJ, 555, 504
Zekser, K. C., et al. 2006, ApJ, 640, 639
Zhao, H. 1996, MNRAS, 278, 488
Zhao, D. H., Jing, Y. P., Mo, H. J., & Börner, G. 2003, ApJ, 597, L9
Zitrin, A., Broadhurst, T., Barkana, R., Rephaeli, Y., & Benitez, N. 2010a, arXiv:1002.0521
Zitrin, A., Broadhurst, T., Rephaeli, Y., & Sadeh, S. 2009a, ApJ, 707, L102
Zitrin, A., et al. 2009b, MNRAS, 396, 1985
Zitrin, A., et al. 2010b, arXiv:1004.4660

Queries

Page 1

Page 3

Page 4

Page 24

Online-only colour figures